Observations of Misovortices within a Long-Lake-Axis-Parallel Lake-Effect Snowband during the OWLeS Project

JAKE P. MULHOLLAND, JEFFREY FRAME, AND STEPHEN W. NESBITT

Department of Atmospheric Sciences, University of Illinois at Urbana–Champaign, Urbana, Illinois

SCOTT M. STEIGER

Department of Atmospheric and Geological Sciences, State University of New York, Oswego, New York

KAREN A. KOSIBA AND JOSHUA WURMAN

Center for Severe Weather Research, Boulder, Colorado

(Manuscript received 12 November 2016, in final form 1 May 2017)

ABSTRACT

Recent lake-effect snow field projects in the eastern Great Lakes region have revealed the presence of misovortices with diameters between 40 and 4000 m along cyclonic horizontal shear zones within long-lake-axis-parallel bands. One particular band in which an abundance of misovortices developed occurred on 7 January 2014. The leading hypothesis for lake-effect misovortexgenesis is the release of horizontal shearing instability (HSI). An analysis of three-dimensional dual-Doppler wind syntheses reveals that two criteria for HSI are satisfied along the horizontal shear zone, strongly suggesting that HSI was the likely cause of the misovortices in this case. Furthermore, the general lack of anticyclonic–cyclonic vortex couplets throughout the event reveal that tilting of horizontal vorticity into the vertical is of less importance compared to the release of HSI and subsequent strengthening via vortex stretching. A WRF simulation depicts misovortices along the horizontal shear zone within the simulated band. The simulated vortices display remarkable similarities to the observed vortices in terms of intensity, depth, spacing, and size. The simulated vortices persist over the eastern end of the lake; however, once the vortices move inland, they quickly dissipate. HSI criteria are also calculated from the WRF simulation and are satisfied along the shear zone. Competing hypotheses of misovortexgenesis are presented, with results indicating that the release of HSI is the likely mechanism of vortex formation.

1. Introduction

Lake-effect snowfall impacts many regions downwind of the Great Lakes every winter, with locations such as the Tug Hill Plateau of upstate New York receiving average annual accumulations over 200 cm. As continental polar air masses cross the Great Lakes, vertical fluxes of heat and moisture from the lake surfaces into the overlying air masses moisten and destabilize the lower boundary layer (BL). This allows for the formation of sometimes vigorous BL convection, often manifested in lake-effect snowbands (e.g., Markowski and Richardson 2010, 93–102). Shore-parallel bands [e.g., Niziol et al. (1995); type-I bands], or more recently and hereafter called long-lake-axis-parallel (LLAP) bands (Steiger et al. 2013), are responsible for the majority of the heaviest snowfall totals downwind of the eastern Great Lakes [Lakes Erie and Ontario; Niziol et al. (1995)].

LLAP bands form when the prevailing BL winds are roughly parallel to the major axis of an elongated lake, allowing for a long fetch and increased moistening and destabilization of the low-level air mass. Additionally, the vertical wind shear vector must be roughly unidirectional with height in the BL for intense LLAP band organization (Niziol 1987). The critical thermodynamic threshold for the formation of lake-effect convection is a 13°C difference between the lake surface water temperature and the overlying 850-hPa air temperature, which results in a nearly dry-adiabatic lapse rate within the BL, fostering the development of sometimes

Corresponding author: Jake P. Mulholland, jmulhol2@illinois.edu

DOI: 10.1175/MWR-D-16-0430.1

© 2017 American Meteorological Society. For information regarding reuse of this content and general copyright information, consult the AMS Copyright Policy (www.ametsoc.org/PUBSReuseLicenses).

Unauthenticated | Downloaded 02/02/24 12:11 AM UTC

TABLE 1. DOW6 and DOW8 (rapid scan) radar specifications during the 7 Jan 2014 event.

	DOW6	DOW8
Half-power beamwidth (°)	0.5	0.8
Frequency (GHz)	9.55	9.3–9.7
Gate length (m)	60	75
Transmitter pulse (ns)	400	1000
Nyquist velocity ($m\,s^{-1}$)	78.47	31.97
Max range (km)	58.5	30
Elevation angles (°)	0.5–14.5	0.5–14.9 (missing 1–2)

significant lake-induced instability [i.e., lake-induced convective available potential energy; Phillips (1972)]. Mobile soundings and model simulations have revealed a warm-core structure within LLAP bands, with low-level convergence near the center of the band, ascent within the core of the band, and divergence atop the band [i.e., an in-up-and-out transverse vertical circulation pattern; e.g., Byrd et al. (1991); Steiger and Ballentine (2008)]. Such low-level convergence zones are common in LLAP bands and may be augmented by land breezes from opposing shores as surrounding land locations are usually colder than the lake surface, especially before sunrise (e.g., Markowski and Richardson 2010, 98–102).

Previous lake-effect research has primarily focused on the western Great Lakes, such as Lakes Michigan and Superior [e.g., the Lake-Induced Convection Experiment (Lake-ICE); Kristovich et al. (2000)]. Some of these studies, including Forbes and Merritt (1984) and Laird et al. (2001), document instances of mesovortices [diameters (D) > 4000 m; Fujita (1981)] forming over the lakes in regimes of weak background synoptic flow [e.g., Niziol et al. (1995); type-V storms]. The formation of mesovortices is largely governed by latent heat release owing to deposition within the bands, inducing rising heights and divergence above the level of maximum heating and falling pressures below this level (e.g., Laird et al. 2001), which in turn fosters low-level cyclonic rotation.

The only previous major field campaign over the eastern Great Lakes was the Lake Ontario Winter Storms (LOWS; Reinking et al. 1993) project, which ran between 5 January and 1 March 1990. Because of a dearth of Arctic air intrusions, however, there was only one documented LLAP band case (12 January 1990). The primary discovery from this field campaign was that the depth of the planetary boundary layer appeared to be a more important indicator of lake-effect band strength than the degree of lake surface-to-850-hPa instability.

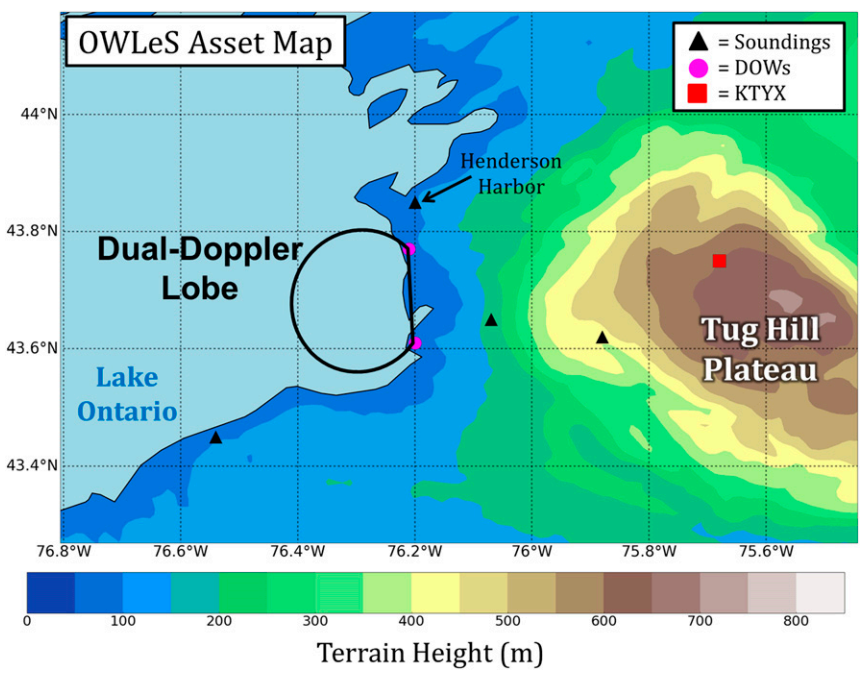

FIG. 1. OWLeS asset map from 7 Jan 2014. The DD lobe from DOW6 and DOW8 is drawn in black; the radar baseline is 16.4 km. The locations of DOW6 and DOW8 are marked with magenta dots (DOW8 to the north; DOW6 to the south), the Montague, NY, WSR-88D (KTYX) location is marked with a red square, and the mobile sounding locations are marked with black triangles.

Unauthenticated | Downloaded 02/02/24 12:11 AM UTC

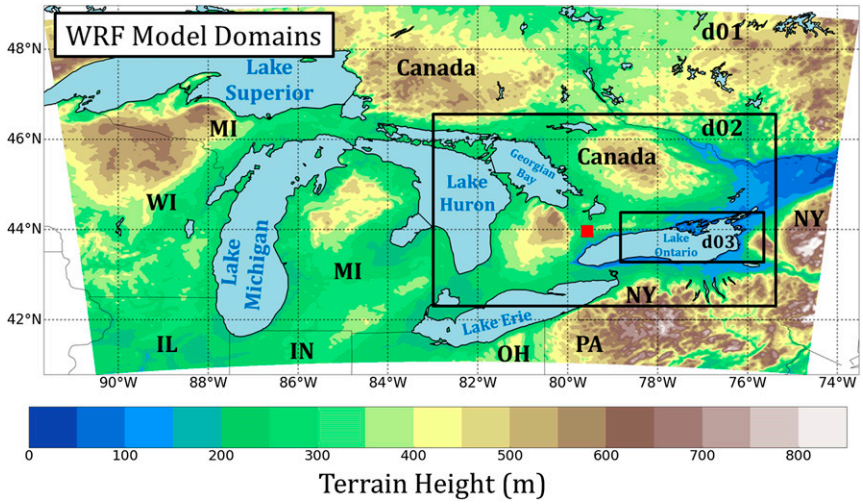

FIG. 2. Domains of the WRF Model simulation. The outermost domain (d01; 1335 km × 882 km) has a horizontal grid spacing of 3 km, the middle domain (d02; 636 km × 438 km) has a horizontal grid spacing of 1 km, while the innermost domain (d03; 258 km × 147 km) has a horizontal grid spacing of 333 m. Terrain height is plotted in meters (shaded). The King City, Ontario (CWKR), radar location is marked with a red square.

A recent field campaign, the Long-Lake-Axis-Parallel (LLAP; Steiger et al. 2013) project, occurred during the winter of 2010/11 across eastern Lake Ontario and featured seven LLAP band cases. The primary goal of the LLAP project was to obtain finescale, dual-polarization, mobile Doppler radar observations of LLAP bands, since conventional Weather Surveillance Radar-1988 Doppler (WSR-88D) coverage across Lake Ontario often suffers from beam overshoot as LLAP bands are typically on the order of 2–4 km deep. Observations of mesovortices ($D > 4000$ m), misovortices ($D = 40$–4000 m), horizontal vortices, horizontal shear zones, bounded weak-echo regions, outflow boundaries, and anvils were all documented (Steiger et al. 2013). Additionally, Steiger et al. (2013) observed that the LLAP bands typically displayed an asymmetric structure with a sharper horizontal reflectivity gradient on either the north or south side of the typically west-to-east-oriented bands. On the same side of the band as the reflectivity gradient, and along the corresponding cyclonic horizontal shear/convergence zone, there were several, roughly evenly spaced, misovortices in some cases. The misovortices were similar to those observed in other field campaigns, such as along drylines across the central Great Plains (e.g., Marquis et al. 2007). The primary formation mechanism for these misovortices was hypothesized to be the release of horizontal shearing instability (HSI; Markowski and Richardson 2010, 58–64) along the shear zone. This hypothesis was not testable, however, since only a single-Doppler radar was available, precluding a dual-Doppler (DD) wind synthesis. No LLAP band cases that the authors are aware of exhibited an anticyclonic shear zone. A more detailed investigation of this hypothesis, along with prior research on HSI-induced vortices, is found in sections 4 and 5.

The largest project of its kind, the Ontario Winter Lake-effect Systems project [OWLeS; Kristovich et al. (2017); data available online at http://data.eol.ucar.edu/master_list/?project=OWLeS], occurred during the winter of 2013/14. Stemming from the successes of the exploratory LLAP project, the OWLeS project sought to examine 1) the kinematics and dynamics of LLAP bands, 2) upwind and downwind lake influences (i.e., heat and moisture fluxes and advection) on lake-effect convection, and 3) orographic influences on lake-effect convection. The original OWLeS proposal planned for eight intensive observation periods (IOPs), whereas 24 IOPs took place, owing to a persistent pattern characterized by high-amplitude ridging across the western United States and deep troughing across the eastern United States (see

TABLE 2. WRF Model specifications. Abbreviations are explained in the text.

Horizontal grid spacing	3 km, 1 km, 333 m
No. of vertical levels	60
Vertical coordinate	η (terrain following)
P_{top}	50 hPa
Microphysical parameterization	Thompson
Boundary layer scheme	Shin–Hong
LW and SW radiation scheme	RRTMG
Surface layer scheme	MM5 Monin–Obukov
Land surface scheme	RUC LSM

Unauthenticated | Downloaded 02/02/24 12:11 AM UTC

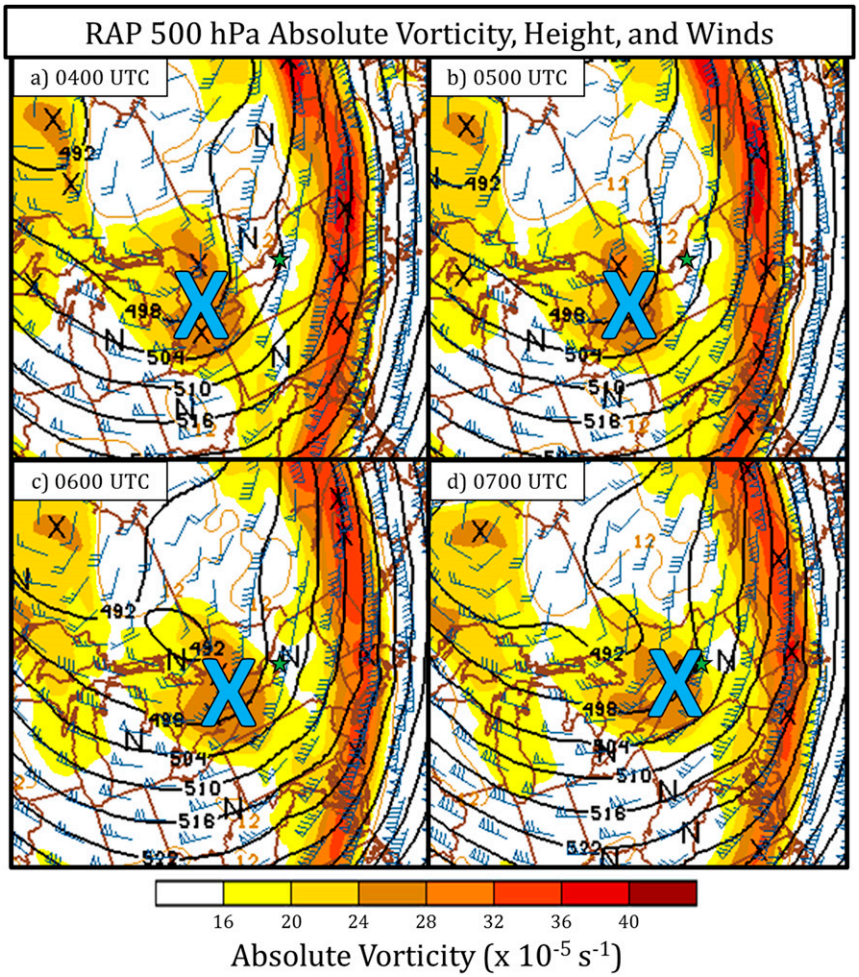

FIG. 3. 500-hPa winds (kt, where 1 kt = 0.5144 m s^{-1}; half barb = 5, full barb = 10, and pennant = 50 kt), geopotential height (contoured every 6 dam), and absolute vertical vorticity ($\times 10^{-5}$ s^{-1}; color fill) from the 0000 UTC 7 Jan 2014 RAP model valid at (a) 0400, (b) 0500, (c) 0600, and (d) 0700 UTC 7 Jan 2014 (courtesy OWLeS field catalog; available online at http://catalog.eol.ucar.edu/owles). The blue "×s" denote vorticity maxima and the black "Ns" denote vorticity minima. The green star denotes the location of a sounding launched from Henderson Harbor (see Fig. 4).

section 3). An abbreviated list of instrumentation utilized during this field campaign is in section 2a.

Similar to the LLAP project, there were many cases during the OWLeS project that featured the presence of misovortices along horizontal shear zones. Thus, the research herein is motivated by and focuses on the first objective of the OWLeS project, and more specifically attempts to understand the processes that aided in the development, maintenance, and demise of the misovortices documented within the 7 January 2014 (IOP7) LLAP band. Steiger et al. (2013), along with OWLeS project field observations, have demonstrated that the larger-scale mesovortices have the ability to alter the morphology of LLAP bands, while the smaller-scale misovortices were typically associated with localized maxima in surface wind speeds and snowfall rates [also noted by Grim et al. (2004)].

Section 2 outlines the data and methods used during this research. Section 3 provides an analysis of the synoptic and mesoscale conditions present on 7 January 2014. Section 4 reveals the dual-Doppler observations of the misovortices. Section 5 includes an analysis of a WRF Model simulation of this band, and a summary and our conclusions are found in section 6.

2. Data and methods

a. Observational data

The platforms that were utilized during the OWLeS project included three X-band Doppler on Wheels

Unauthenticated | Downloaded 02/02/24 12:11 AM UTC

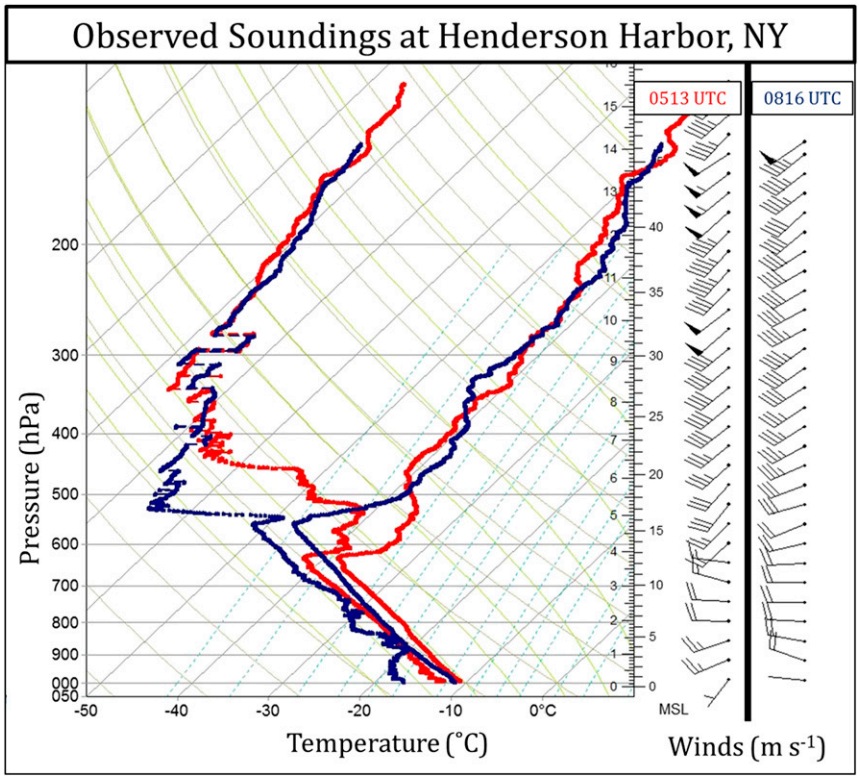

FIG. 4. Soundings launched at 0513 UTC (red) and 0816 UTC (blue) 7 Jan 2014 from Henderson Harbor. Horizontal winds ($m\,s^{-1}$; half barb = 5, full barb = 10, and pennant = $50\,m\,s^{-1}$) for both soundings are plotted along the right side of the image.

(DOW; Wurman et al. 1997) radars (two dual-polarization units), five (four mobile) rawinsonde systems, the University of Wyoming King Air (UWKA) aircraft (Rodi 2011), four Micro Rain Radars (MRRs; Minder et al. 2015), and the University of Alabama in Huntsville's Mobile Integrated Profiling System (MIPS; Karan and Knupp 2006). Radar data from 7 January 2014 were collected using two mobile X-band DOW radars, the specifications for which are listed in Table 1. The radars were deployed between 0200 and 2230 UTC 7 January 2014. DOW6 was stationed at Rainbow Shores, New York, while DOW8 was stationed at Southwick Beach, New York, resulting in a DD lobe over eastern Lake Ontario (Fig. 1; radar baseline of 16.4 km). The locations of the assets utilized during this research are depicted in Fig. 1.

b. Dual-Doppler specifications

Raw DOW data were first subjectively edited using NCAR Solo3 software (Bell et al. 2013). All radar data east of Lake Ontario were removed owing to beam blockage resulting from tree cover. Using a cross-correlation coefficient [ρ_{HV}; Fabry (2015, 99–101)] minimum threshold of 0.94 [which, according to Fabry (2015), is representative of nonmeteorological targets in a typical dry snow environment], ground clutter within the DOW6 dataset was removed, including sea spray/clutter, the shoreline imprint of Lake Ontario, buildings, trees, and other nonmeteorological targets. A similar editing process was applied to data from DOW8; however, since DOW8 is not a dual-polarization radar, ground clutter was filtered using high reflectivity (25+ dBZ used as a threshold), collocated with $<|2|\,m\,s^{-1}$ radial velocity magnitudes that were clearly not associated with precipitation. Other noise was removed by thresholding on the normalized coherent power (NCP; Dixon and Hubbert 2012). An NCP value of 0.30 was used to identify regions of low signal. The core of the vortices typically displayed low NCP magnitudes owing to turbulence, so these areas were left unchanged, and all remaining data with NCP magnitudes below 0.30 were removed. All other nonmeteorological targets or noise that remained were manually removed at the conclusion of the editing process.

Using a two-pass Barnes objective analysis scheme (Barnes 1964), with a second-pass convergence parameter γ of 0.30 (Majcen et al. 2008), the edited radar data were mapped onto a 40 km × 40 km × 2.5 km Cartesian

Unauthenticated | Downloaded 02/02/24 12:11 AM UTC

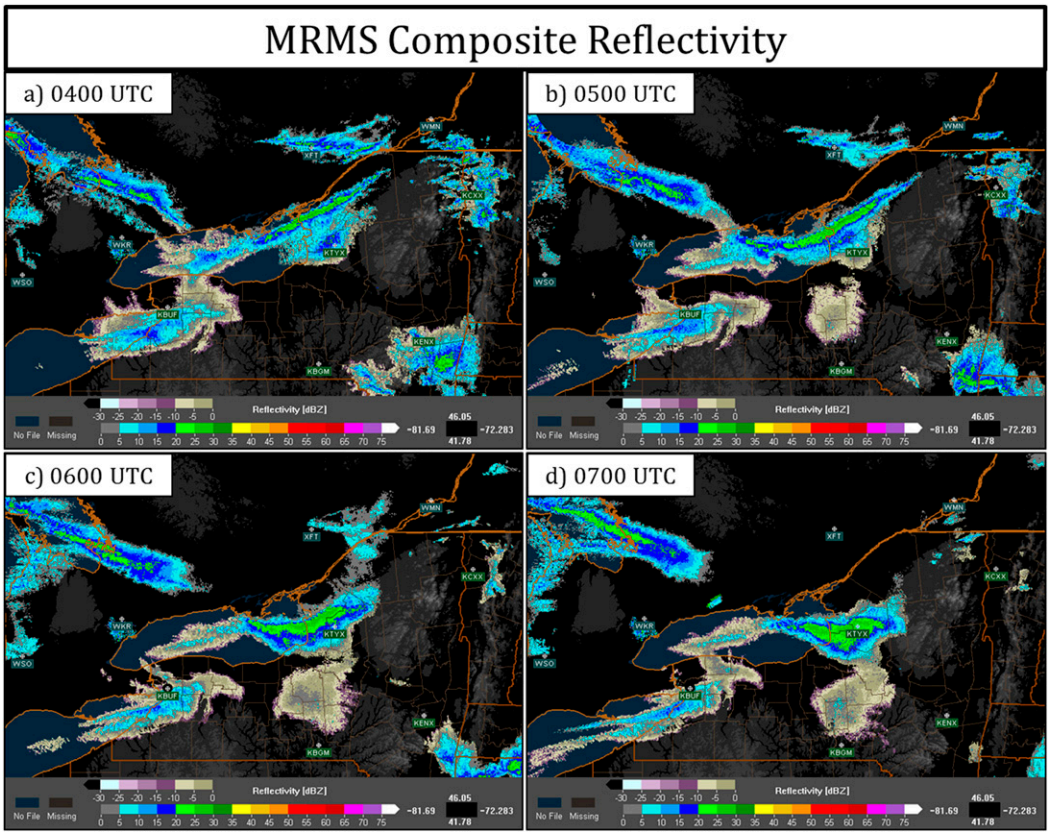

FIG. 5. Multi-Radar Multi-Sensor System (MRMS; information online at http://mrms.ou.edu/) composite reflectivity (dBZ; shaded) and terrain (grayscale background) valid at (a) 0400, (b) 0500, (c) 0600, and (d) 0700 UTC 7 Jan 2014.

grid with horizontal and vertical grid spacing of 250 m, consistent with recommendations of Pauley and Wu (1990), where Δx, Δy, $\Delta z = 5\delta/12$, and $\delta = (\text{beamwidth})(\pi/180°)(X)$, where X is the greatest distance from one of the radars to a feature of interest (in kilometers). The Barnes smoothing parameter is given by $K = (1.33\delta)^2$, which is also consistent with recommendations by Pauley and Wu (1990) and Marquis et al. (2007). The horizontal smoothing parameter (K_H) was 0.747 km^2 while the vertical smoothing parameter (K_Z) was 0.400 km^2. Elevation scans between 1° and 2° from DOW8 were missing because one of the beams was nonfunctional, necessitating the difference in the horizontal and vertical smoothing parameters mentioned above. The origin of the Cartesian grid was the location of DOW6. No downward interpolation was performed during the objective analysis. Three-dimensional wind syntheses were obtained from the objectively analyzed radar data by integrating the anelastic mass continuity equation upward from the bottom of the domain, using software provided by the Center for Severe Weather Research [CSWR; see the appendix of Kosiba et al. (2013)], assuming $w = 0$ at the bottom of the domain. The DD wind syntheses were subjected to a downward interpolation method, discussed in detail in the appendix of Kosiba et al. (2013). From these DD wind syntheses, fields such as vertical vorticity and horizontal divergence were calculated and analyzed. Given the inherent uncertainties in utilizing the integration of the anelastic mass continuity equation upward from the surface at an increasing range from the radar, magnitudes of vertical velocity and horizontal divergence should be interpreted with caution. These particular fields, which are presented in section 4, are analyzed to illustrate their positioning relative to individual vortices. For example, many updrafts overlap with vortices, indicating that vortex stretching is likely occurring. Exact magnitudes of vertical velocity, horizontal divergence, and stretching should be interpreted cautiously, however.

c. *Weather Research and Forecasting Model specifications*

A Weather Research and Forecasting (WRF) Model simulation using the Advanced Research core (WRF-ARW;

Unauthenticated | Downloaded 02/02/24 12:11 AM UTC

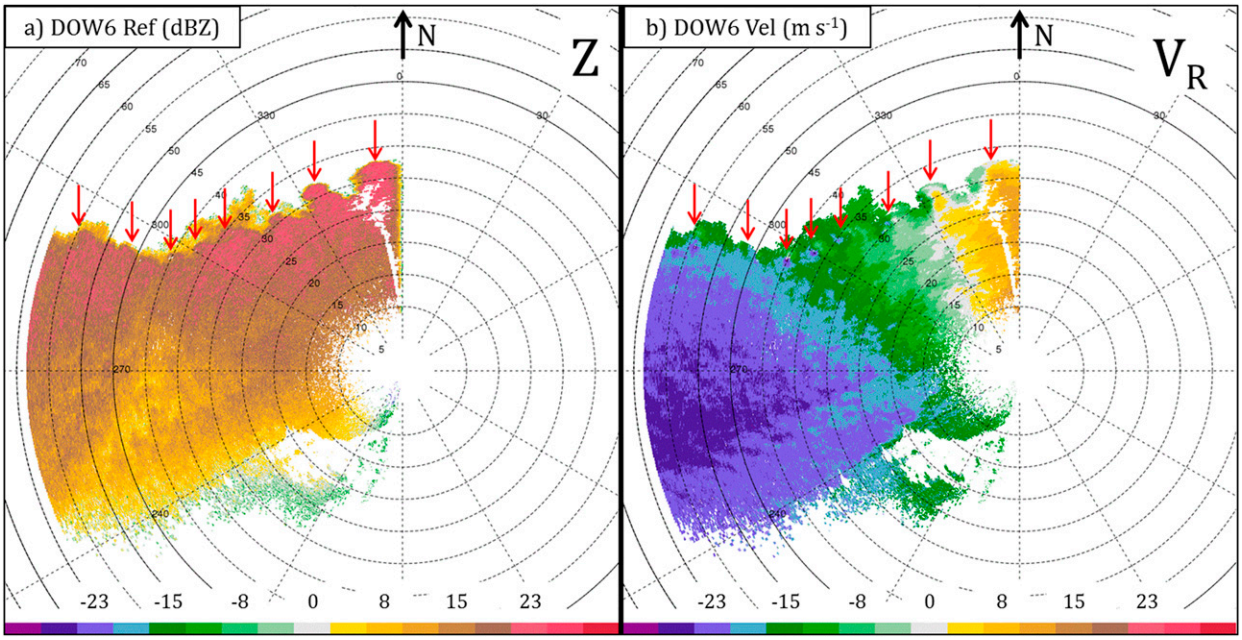

FIG. 6. The 0.4° DOW6 (a) reflectivity (dBZ) and (b) radial velocity (m s^{-1}) at 0523:55 UTC 7 Jan 2014. Range rings are plotted every 5 km and azimuth angles are plotted every 30°. Each misovortex is denoted by a red arrow.

version 3.7.1) was conducted for this case. The innermost grid has a horizontal resolution of 333 m (258 km × 147 km) and is nested within 1-km (636 km × 438 km) and 3-km (1335 km × 882 km) grids (Fig. 2). The outermost domain (3-km horizontal resolution) was initialized from the 0000 UTC 7 January 2014 Rapid Refresh (RAP) model. Lake surface water temperatures were directly prescribed from the RAP model. The 3-km domain was used to capture the synoptic-scale features across the Great Lakes, while the 1-km domain was centered on Georgian Bay and Lake Ontario to capture a connection between the LLAP band originating over Georgian Bay and that over Lake Ontario (see section 3). The finest-scale (333 m) domain only encompassed eastern Lake Ontario to reproduce the misovortices, which were observed in the mobile radar data. The 333-m grid spacing is comparable to the 250-m horizontal resolution of the DD grid, allowing for a nearly one-to-one comparison of vortex characteristics including strength, spacing, speed, and depth; although, the effective resolution of both of the WRF simulation and the DD analyses are significantly lower than 333 and 250 m, respectively (e.g., Skamarock 2004).

The model simulation utilized 60 vertical levels with a terrain-following eta coordinate. The top of the model domain was at 50 hPa (~20 km AGL). No damping layer was implemented near the model top owing to the relatively shallow depth of the band (<5 km AGL) and short duration of the model integration (12 h). A vertically stretched grid was utilized, with the lowest model level located at 75 m AGL. The vertical grid spacing near the surface is 75 m and decreases to approximately 750 m near the model top. The model was run on the Arakawa C grid and Runge–Kutta second- and third-order time integration schemes were utilized. The Thompson microphysical scheme (Thompson et al. 2008) was utilized along with the Rapid Radiative Transfer Model for GCMs (RRTMG) longwave and shortwave radiation schemes (Iacono et al. 2008), the Rapid Update Cycle (RUC) land surface model (LSM; Smirnova et al. 2016), the revised Pennsylvania State University–National Center for Atmospheric Research (PSU–NCAR) Mesoscale Model (MM5) Monin–Obukov surface-layer scheme (Jiménez et al. 2012), and the new Shin–Hong (Shin and Hong 2015) BL parameterization. No cumulus parameterization scheme was implemented at any grid scale. A summary of the model configuration is found in Table 2.

3. Synoptic overview of 7 January 2014

Throughout the winter of 2013/14, frequent intrusions of Arctic air masses occurred over most of the eastern United States. One such event took place between 6 and 9 January 2014, with some locations east of Lake Ontario receiving over 125 cm of fresh lake-effect snowfall. The 0000 UTC 7 January 2014 RAP model 500-hPa analysis reveals a short-wave trough west of

Unauthenticated | Downloaded 02/02/24 12:11 AM UTC

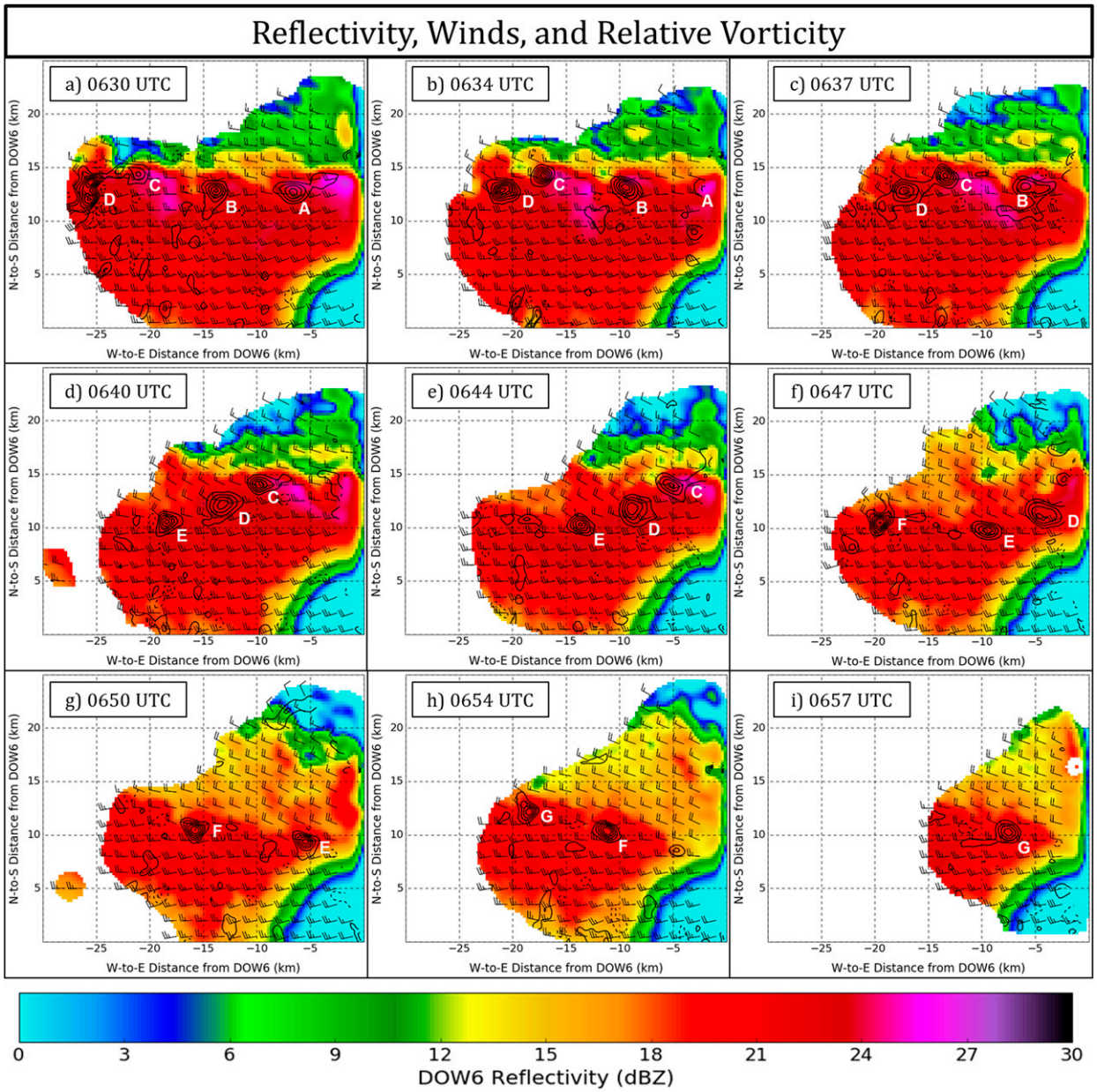

FIG. 7. DD wind syntheses at 500 m AGL with horizontal winds ($m\,s^{-1}$; half barb = 5, full barb = 10 $m\,s^{-1}$), DOW6 composite reflectivity (dBZ; shaded), and vertical vorticity (contoured every $0.5 \times 10^{-2}\,s^{-1}$ starting at $-5.5 \times 10^{-2}\,s^{-1}$; solid = positive and dashed = negative) valid at (a) 0630, (b) 0634, (c) 0637, (d) 0640, (e) 0644, (f) 0647, (g) 0650, (h) 0654, and (i) 0657 UTC 7 Jan 2014. Each misovortex is labeled with a capital letter between A and G. The y axis is the north–south distance in km from DOW6 and the x axis is the east–west distance in km from DOW6.

Lake Ontario (denoted by the blue × in Fig. 3), which traversed the lake between 0400 and 0800 UTC. Quasigeostrophic ascent due to differential cyclonic vorticity advection ahead of this trough overspread the lake, allowing the capping inversion atop the Arctic air mass to rise. Soundings launched at 0513 and 0816 UTC from Henderson Harbor, New York (green star in Fig. 3), depict cooling below 500 hPa and the vertical extension of the BL in association with the synoptic-scale ascent (Fig. 4). The 0816 UTC sounding reveals a moist and conditionally unstable BL extending vertically to nearly 540 hPa (Fig. 4). With 850-hPa temperatures around −25°C, lake surface water temperatures around 3°C (not shown), and a nearly unidirectional wind

Unauthenticated | Downloaded 02/02/24 12:11 AM UTC

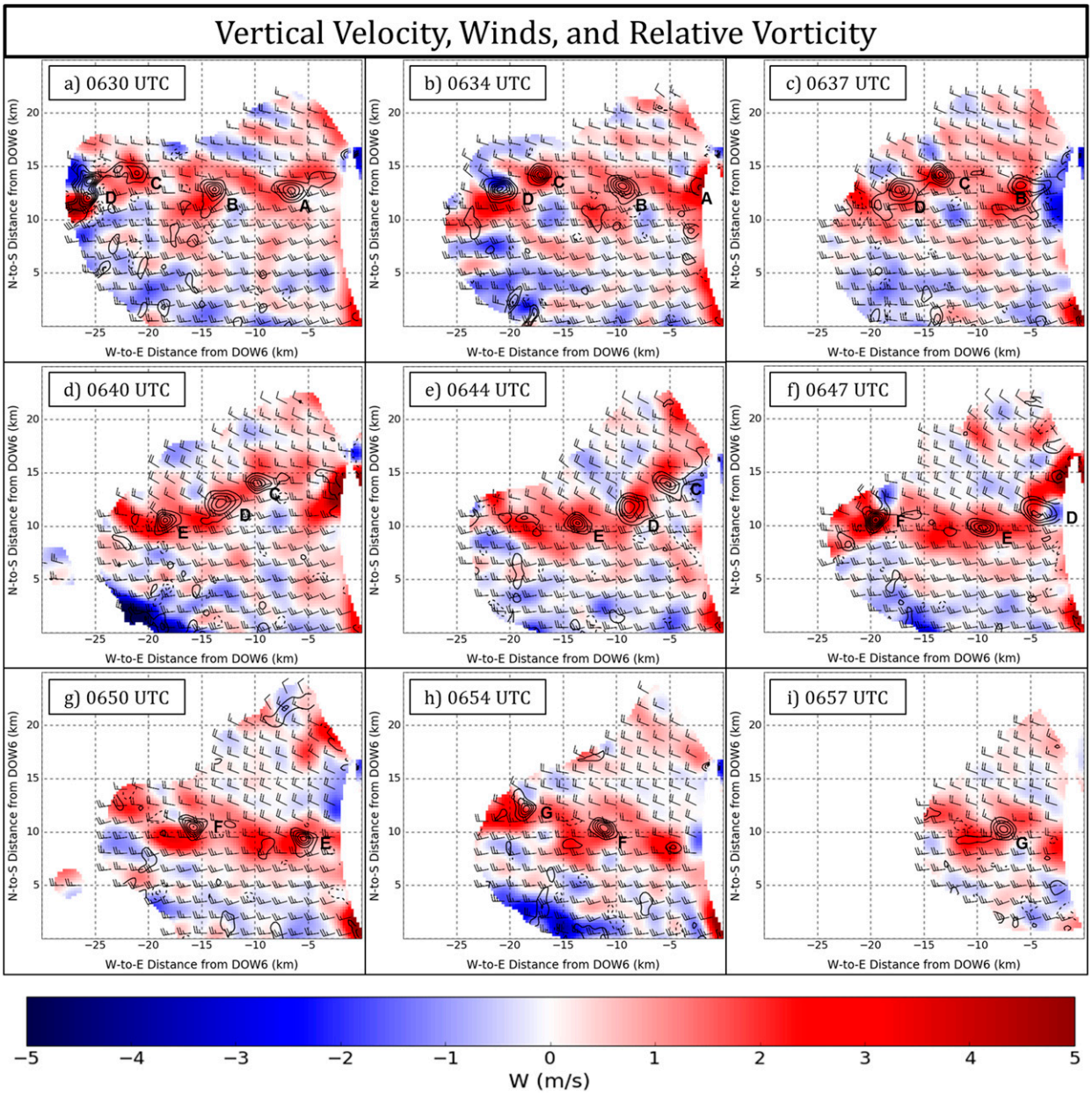

FIG. 8. DD wind syntheses at 500 m AGL with horizontal winds ($m\,s^{-1}$; half barb = 5 and full barb = $10\,m\,s^{-1}$), vertical vorticity (contoured every $0.5 \times 10^{-2}\,s^{-1}$ starting at $-5.5 \times 10^{-2}\,s^{-1}$; solid = positive and dashed = negative), and vertical velocity ($m\,s^{-1}$; color filled) valid at (a) 0630, (b) 0634, (c) 0637, (d) 0640, (e) 0644, (f) 0647, (g) 0650, (h) 0654, and (i) 0657 UTC 7 Jan 2014. Each misovortex is labeled with a capital letter between A and G. The *y* axis is the north–south distance in km from DOW6 and the *x* axis is the east–west distance in km from DOW6.

profile in the BL, thermodynamic and kinematic conditions were more than adequate for an intense LLAP band to develop over Lake Ontario (Fig. 5).

Further inspection of the mesoscale regime revealed a connection [identified by horizontal extrapolation of upstream radar echoes indicating the advection of lake-modified, boundary layer air; see Kristovich et al. (2017)] between the Lake Ontario band and another LLAP band upstream over Georgian Bay between 0400 and 0800 UTC (Fig. 5). This connection ceased after 0800 UTC, as BL winds over Georgian Bay backed from northwesterly to westerly following the passage of the aforementioned 500-hPa short-wave trough and the approach of a 700-hPa ridge from the west

Unauthenticated | Downloaded 02/02/24 12:11 AM UTC

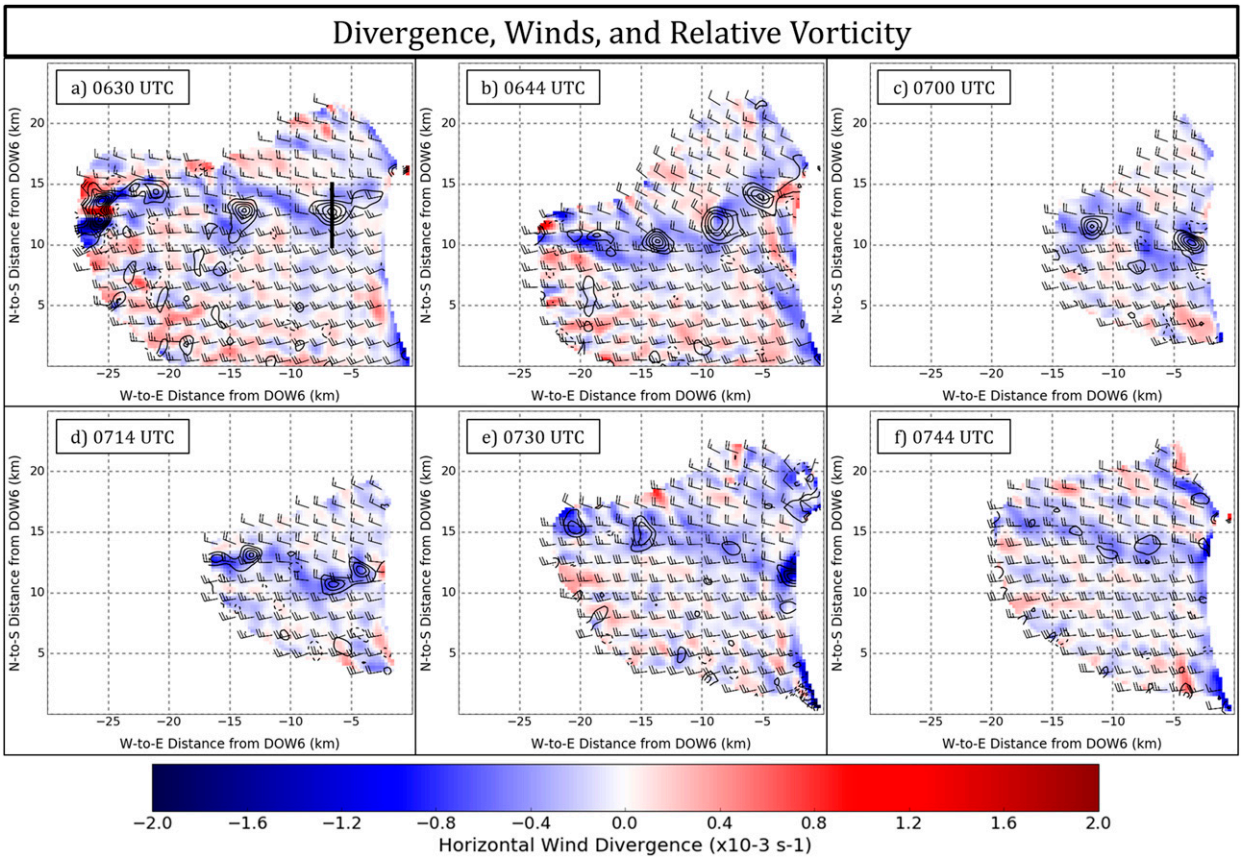

FIG. 9. DD wind syntheses at 500 m AGL with horizontal wind divergence (color filled every $0.4 \times 10^{-3}\,\mathrm{s}^{-1}$), horizontal winds ($\mathrm{m\,s}^{-1}$; half barb = 5 and full barb = $10\,\mathrm{m\,s}^{-1}$), and vertical vorticity (contoured every $0.5 \times 10^{-2}\,\mathrm{s}^{-1}$ starting at $-5.5 \times 10^{-2}\,\mathrm{s}^{-1}$; solid = positive and dashed = negative) valid at (a) 0630, (b) 0644, (c) 0700, (d) 0714, (e) 0730, and (f) 0744 UTC 7 Jan 2014. The black line in (a) denotes the south-to-north vertical cross section displayed in Fig. 10.

(see section 5a). Multilake connections are commonly observed across the Great Lakes during instances of northwest BL flow in which a single snow/cloud band may be traced across as many as three lakes (e.g., Byrd et al. 1991; Sousounis and Mann 2000; Rodriguez et al. 2007).

The Lake Ontario LLAP band persisted for over 20 h on 6–7 January 2014, even after the upstream connection was lost. Analyses in sections 4 and 5 are focused between 0400 and 0800 UTC (0900 UTC for the WRF simulation) since this was when a string of misovortices was present. Isolated vortices were observed after 0800 UTC, but strings of vortices were not documented after this time.

4. Dual-Doppler analyses

a. Vortex characteristics

A string of misovortices was observed within the LLAP band between 0400 and 0800 UTC. Figure 6 depicts these vortices at 0524 UTC, with diameters [defined here as the distance between the local maximum–minimum values of radial velocity that are coincident with a maximum in vertical vorticity, as in Steiger et al. (2013)] ranging from 1 to 3 km and an average horizontal spacing of 6.6 km. The misovortices were located along the northern edge of the band, near a sharp north–south horizontal gradient in reflectivity (Fig. 6).

Figure 7 displays a 27-min (0630–0657 UTC), DD-derived time evolution of the string of misovortices (labeled with capital letters, A–G). The vortices throughout this time period did not interact with one another and could be tracked for greater than 30 min. The region along which the vortices developed was characterized by a cyclonic horizontal shear zone, evidenced by faster westerly wind speeds (on the order of $25\,\mathrm{m\,s}^{-1}$), south of the shear zone, and slower westerly wind speeds (on the order of $15\,\mathrm{m\,s}^{-1}$), north of the shear zone (Fig. 7). Locally stronger westerly winds were observed south of the cyclonic vortices, with weaker westerly winds to the north. Vertical vorticity values

Unauthenticated | Downloaded 02/02/24 12:11 AM UTC

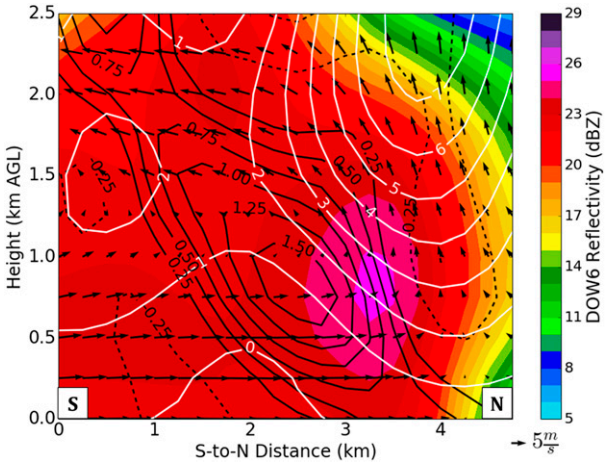

FIG. 10. South-to-north vertical cross section through vortex A at 0630 UTC along the black line in Fig. 9. DOW6 reflectivity (dBZ; color filled), vertical velocity (only positive values plotted; white contours every 1 m s^{-1} starting at 0 m s^{-1}), vertical vorticity (contoured every 0.25×10^{-2} s^{-1} starting at -5.5×10^{-2} s^{-1}; solid = positive and dashed = negative; zero contour suppressed), and wind vectors (v and w components only; m s^{-1}) are plotted.

within the vortices ranged from 1 to 3×10^{-2} s^{-1}, which are values within the range of those documented in previous studies of misovortices (e.g., Mueller and Carbone 1987; Wilson et al. 1992; Lee and Wilhelmson 1997; Kawashima and Fujiyoshi 2005; Arnott et al. 2006; Buban et al. 2007; Marquis et al. 2007; Campbell et al. 2014). Vortices A–E were tracked at successive times between 0630 and 0657 UTC and exhibited an average propagation speed of 19 m s^{-1} toward the east-southeast (ESE). The string of vortices appears to travel with the mean zonal wind within the vortex-bearing layer, which in this case was determined to be 0–2 km AGL (not shown). The average horizontal spacing between the vortices was approximately 5.6 km, which is roughly 1 km less than at 0524 UTC (Fig. 6).

Updrafts along the shear zone range between 1 and 3 m s^{-1} at 500 m AGL, with some isolated stronger updrafts present (Fig. 8). In some instances, the center of an updraft overlapped with a misovortex (e.g., Fig. 8b; vortex C), but in other instances the updraft and vortex were separated (e.g., Fig. 8g; vortex F). Regions of locally enhanced low-level convergence and upward motion were generally located northeast (NE) and southwest (SW) of each vortex, with the strongest vortices exhibiting near-zero convergence (or sometimes weak divergence) within their cores, while weaker vortices exhibited more uniform convergence within their cores (Figs. 8 and 9). Magnitudes of convergence along the wind shift range between 1 and 2×10^{-3} s^{-1} (Fig. 9). This observation is similar to the results of Marquis et al. (2007), whose conceptual model of a convergence boundary superposed with misovortices matches the findings in the present study (see their Fig. 14). This convergence configuration relative to the vortices has been noted in other studies of misovortices as well, including Kingsmill (1995) and Lee and Wilhelmson (1997).

A representative north–south vertical cross section through vortex A at 0630 UTC is depicted in Fig. 10 (taken along the black line in Fig. 9). A transverse secondary circulation pattern associated with the

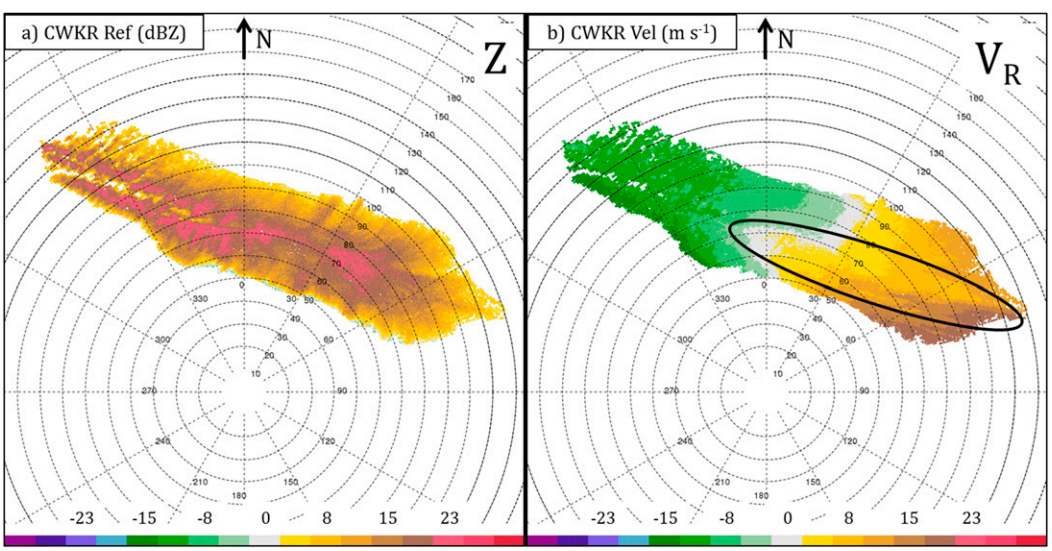

FIG. 11. The 0.2° CWKR (red square in Fig. 2) (a) reflectivity (dBZ) and (b) radial velocity (m s^{-1}) at 0523:35 UTC 7 Jan 2014. Range rings are plotted every 10 km and azimuth angles are plotted every 30°. The black oval denotes the location of the cyclonic horizontal shear zone discussed in the text.

Unauthenticated | Downloaded 02/02/24 12:11 AM UTC

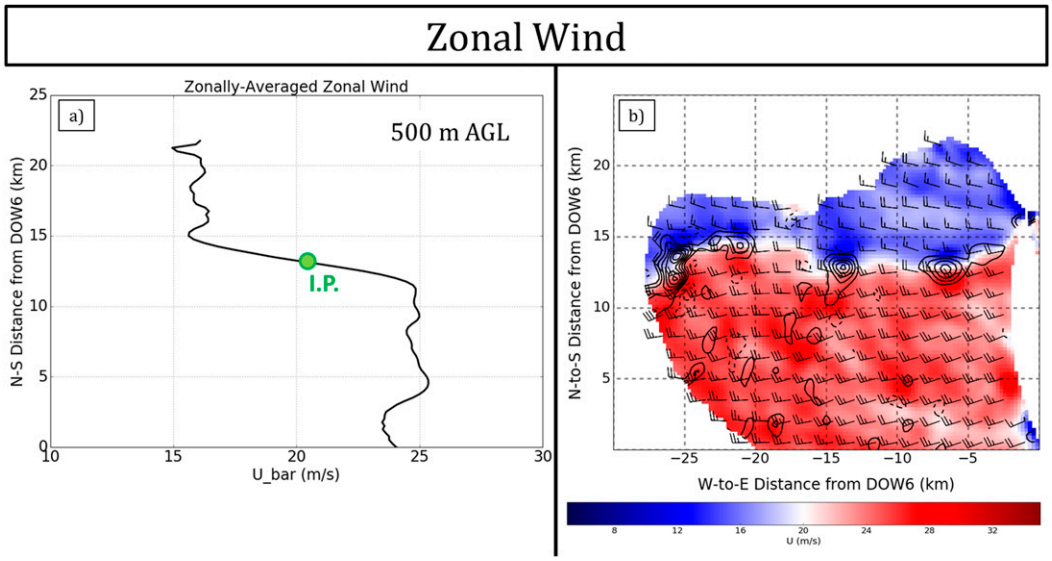

FIG. 12. DD wind synthesis at 500 m AGL valid at 0630 UTC 7 Jan 2014 with (a) $\overline{u}$ profile (m s^{-1}) vs north–south distance (km) from DOW6 and (b) zonal horizontal wind speed (m s^{-1}; color filled), horizontal winds (m s^{-1}; half barb = 5 and full barb = 10 m s^{-1}), and vertical vorticity (contoured every 0.5×10^{-2} s^{-1} starting at -5.5×10^{-2} s^{-1}; solid = positive and dashed = negative). The green dot in (a) denotes the average zonal wind at the inflection point ($\overline{u}_I$).

lake-effect band is present, extending to at least 2 km AGL (Fig. 10). This circulation is manifest by near-surface convergence, ascent, and band-top divergence (see also section 5b). This vortex is strongest between 0.5 and 1.25 km AGL, with vertical vorticity magnitudes greater than 1.0×10^{-2} s^{-1}, and weakens with height above 1.25 km. This vortex tilts toward the south with height because winds above 1.25 km AGL become increasingly

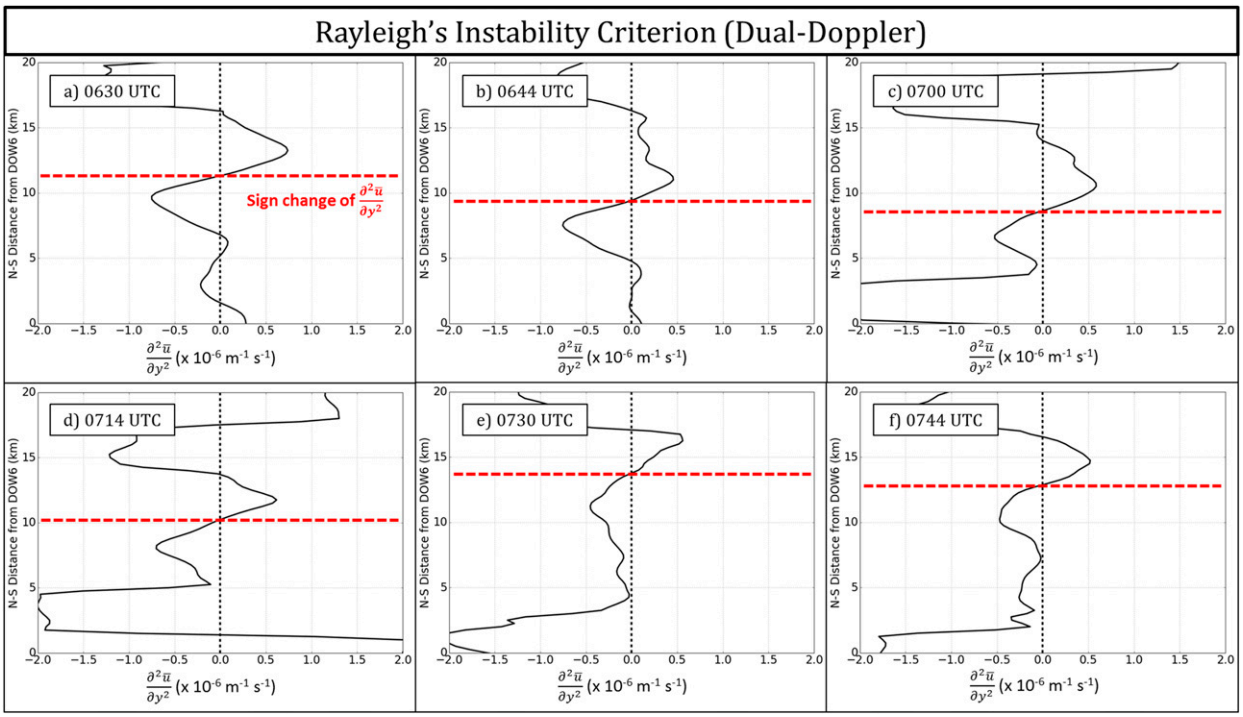

FIG. 13. The quantity $\partial^2\overline{u}/\partial y^2$ ($\times 10^{-6}$ m^{-1} s^{-1}) vs north–south distance (km) from DOW6 at 500 m AGL valid at (a) 0630, (b) 0644, (c) 0700, (d) 0714, (e) 0730, and (f) 0744 UTC 7 Jan 2014. The red dashed lines denote the locations where RIC is satisfied.

Unauthenticated | Downloaded 02/02/24 12:11 AM UTC

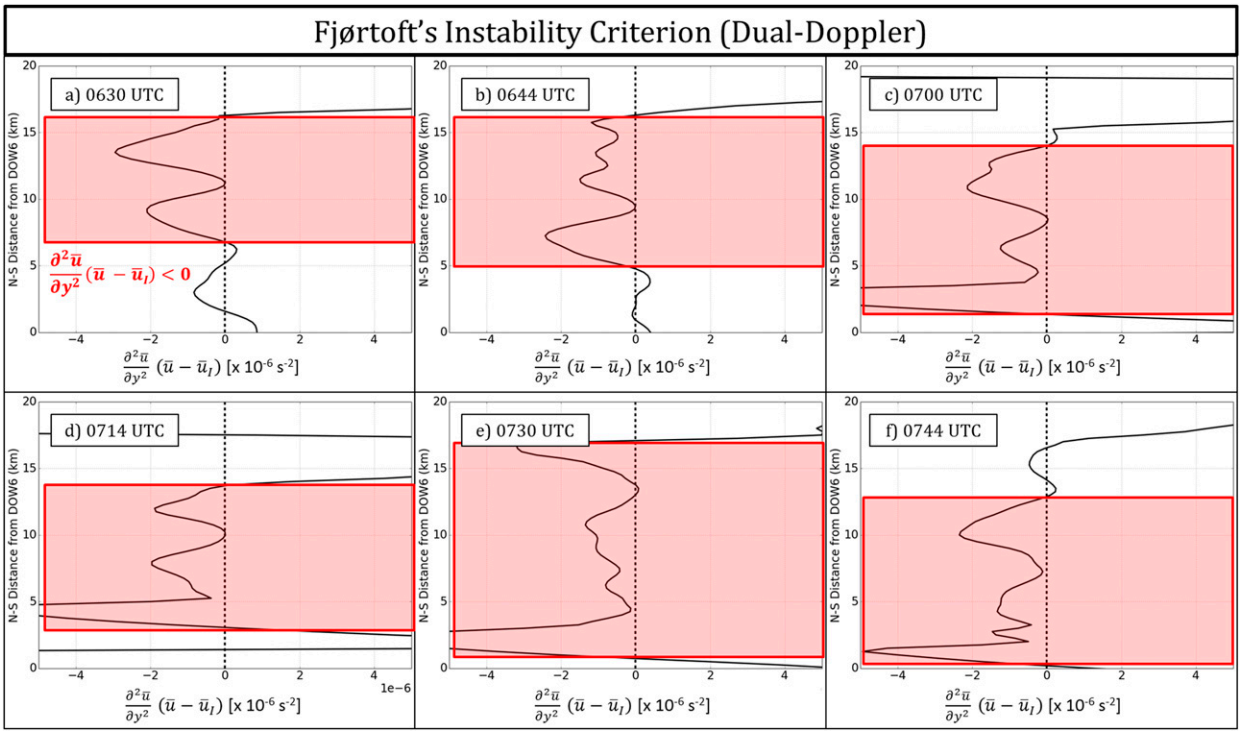

FIG. 14. The quantity $(\partial^2\overline{u}/\partial y^2)(\overline{u} - \overline{u}_I)$ ($\times 10^{-6}\,\mathrm{s}^{-2}$) vs north–south distance (km) from DOW6 at 500 m AGL valid at (a) 0630, (b) 0644, (c) 0700, (d) 0714, (e) 0730, and (f) 0744 UTC 7 Jan 2014. The red shaded rectangles indicate where FIC is satisfied.

northerly near the top of the band (Fig. 10). Although the updraft is slightly north of the vortex, however, updraft magnitudes between 1 and 3 m s^{-1} overlap with vertical vorticity values greater than $1.0 \times 10^{-2}\,\mathrm{s}^{-1}$. The juxtaposition between low-level upward motion and vertical vorticity further enhances the vertical vorticity via stretching. Most of the vortices are offset from updrafts, however, possibly owing to a relatively muted second mechanism (of tilting) in which the dominant cyclonic (much weaker anticyclonic) vortex is to the south (north) of the main updraft (e.g., Fig. 10). It is also possible that the vortices could locally enhance the vertical motion field through augmentation of low-level convergence to the NE and SW of each vortex center (e.g., Marquis et al. 2007, their Fig. 14).

By 0744 UTC (Fig. 9f), the lack of a string of vortices is noted, which is in stark contrast to what was observed around 0630 UTC (Fig. 9a) and even earlier (not shown). The vertical vorticity and horizontal convergence values decreased along the shear zone at 0744 UTC and were only on the order of 0.5–1.0 $\times 10^{-2}\,\mathrm{s}^{-1}$ and 0.4–0.8 $\times 10^{-3}\,\mathrm{s}^{-1}$ (Fig. 9f), respectively. Vertical velocity values had also decreased to around 1 m s^{-1}, from earlier values between 1.5 and 3.0 m s^{-1} (not shown). This decrease in the updraft strength likely restricted the subsequent amplification of the vortices via stretching.

This transition to a regime characterized by a general lack of vortices also followed the passage of the 500-hPa short-wave trough and the approach of the 700-hPa ridge, resulting in the termination of the connection with Georgian Bay (as discussed in section 3). The string of misovortices over Lake Ontario in this particular case may have been influenced by Georgian Bay; once the upstream connection ceased, the string of misovortices vanished and instances of only isolated vortices prevailed throughout the remainder of the event. Observations from the King City, Ontario, radar (CWKR; red square in Fig. 2) depict a cyclonic horizontal shear zone downwind of Georgian Bay, oriented southeastward toward Lake Ontario (Fig. 11). Analyses from a WRF simulation of the morphology of this cyclonic horizontal shear zone are presented in section 5.

b. *Horizontal shearing instability*

The development of strings of misovortices along horizontal wind shifts has been attributed to the release of HSI in previous observational (e.g., Mueller and Carbone 1987; Marquis et al. 2007) and modeling (e.g., Lee and Wilhelmson 1997; Buban and Ziegler 2016) studies. In an attempt to support the hypothesis that HSI was the main driver for the development of the misovortices in this case, two HSI criteria were analyzed. For

Unauthenticated | Downloaded 02/02/24 12:11 AM UTC

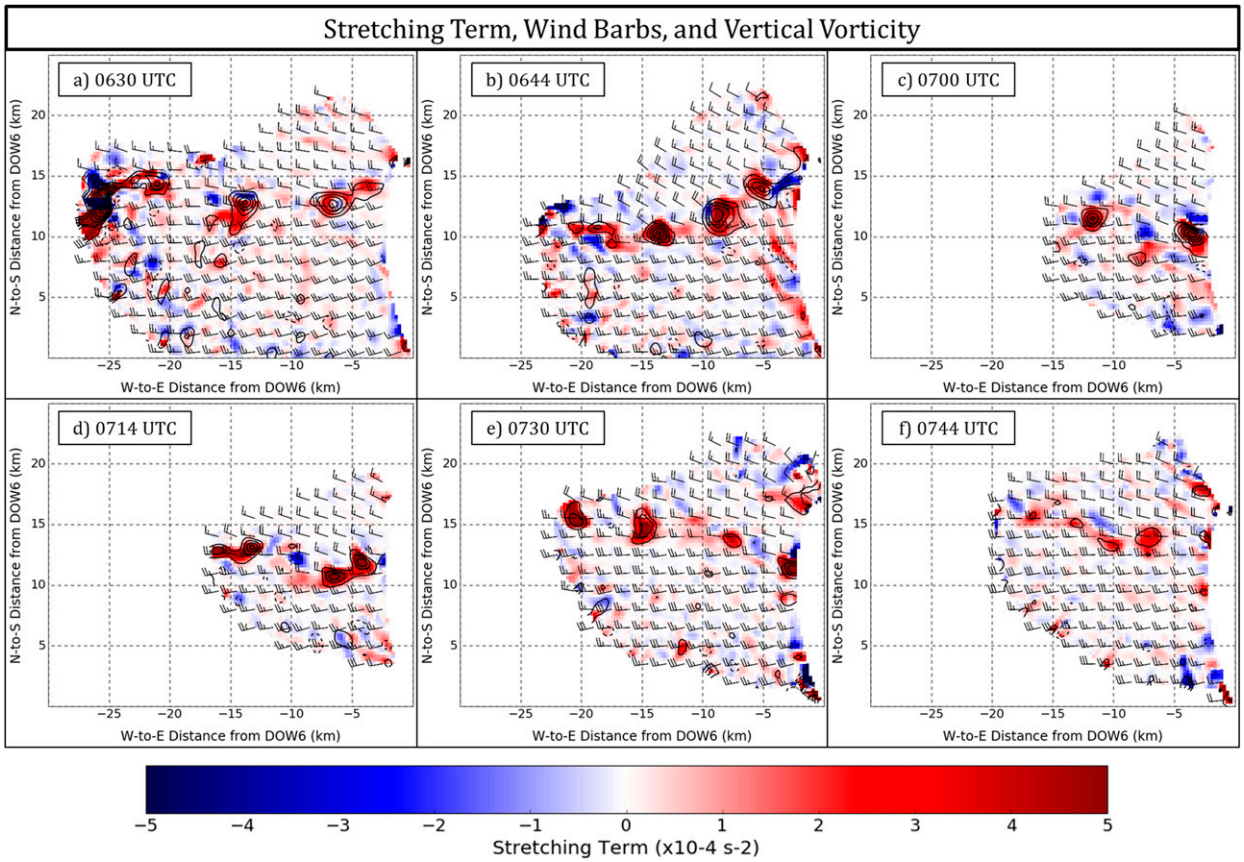

FIG. 15. DD wind syntheses at 500 m AGL displaying the stretching term ($\times 10^{-4}\,\mathrm{s}^{-2}$; shaded), horizontal winds ($\mathrm{m\,s}^{-1}$; half barb = 5 and full barb = $10\,\mathrm{m\,s}^{-1}$), and vertical vorticity (contoured every $0.5 \times 10^{-2}\,\mathrm{s}^{-1}$ starting at $-5.5 \times 10^{-2}\,\mathrm{s}^{-1}$; solid = positive and dashed = negative) valid at (a) 0630, (b) 0644, (c) 0700, (d) 0714, (e) 0730, and (f) 0744 UTC 7 Jan 2014.

HSI to be present, $\beta - (\partial^2\overline{u}/\partial y^2)$ must change sign somewhere within the flow [see Markowski and Richardson (2010), 63–64, for a full derivation], where $\beta = \partial f/\partial y$, f is the Coriolis parameter, y is the meridional direction, and $\overline{u}$ is the wind component parallel to the wind shift averaged along the wind shift. Assuming $f = 10^{-4}\,\mathrm{s}^{-1}$ and $y = 10^7\,\mathrm{m}$ (approximate distance from equator to either pole), β is of order $10^{-11}\,\mathrm{m}^{-1}\,\mathrm{s}^{-1}$. A scale analysis of the quantity, $\partial^2\overline{u}/\partial y^2$, using an approximate $\Delta\overline{u} = 10\,\mathrm{m\,s}^{-1}$ and $\Delta y = 10^4\,\mathrm{m}$, results in a value on the order of $10^{-7}\,\mathrm{m}^{-1}\,\mathrm{s}^{-1}$ (approximately four orders of magnitude larger than β). Hence, we can ignore β, leaving the sign change of $\partial^2\overline{u}/\partial y^2$ as Rayleigh's instability criterion (RIC; Rayleigh 1880). A more stringent instability criterion, derived by Fjørtoft (1950; hereafter FIC), states that $(\partial^2\overline{u}/\partial y^2)(\overline{u} - \overline{u}_I) < 0$ for instability, where $\overline{u}_I$ is the mean base-state wind shift–parallel wind at the inflection point (found from plotting $\overline{u}$ versus y at each analysis time; e.g., see Fig. 12). These are both necessary, but insufficient conditions for instability, however.

Figure 12a, at 0630 UTC, depicts the $\overline{u}$ profile (as a function of y) with an inflection point (green dot labeled I.P.) at $y = 13\,\mathrm{km}$. This inflection point corresponds to the location of the shear zone and vortices in Fig. 12b. There is also a sign change in $\partial^2\overline{u}/\partial y^2$ at $y = 11\,\mathrm{km}$ (Fig. 13a). Hence, RIC is met along the shear zone at 0630 UTC. There are other locations that satisfy RIC, such as at $y = 2\,\mathrm{km}$ (Fig. 13a); however, this is not within the shear zone and may result from noise near the edges of the DD domain. A triangular-weighted smoother (Wittenberg 2009) was applied to the initial $\overline{u}$ field to reduce some of this smaller-scale noise resulting from calculating higher-order derivatives.

Inspection of RIC between 0644 and 0744 UTC (Figs. 13b–f) reveals that this instability criterion is met at each successive time with a clear sign change of $\partial^2\overline{u}/\partial y^2$ near the horizontal shear zone and vortices (red dashed lines in Fig. 13). The fact that this instability criterion was satisfied along the shear zone at each analysis time strongly supports the hypothesis that HSI was the primary mechanism for misovortexgenesis in this case.

Unauthenticated | Downloaded 02/02/24 12:11 AM UTC

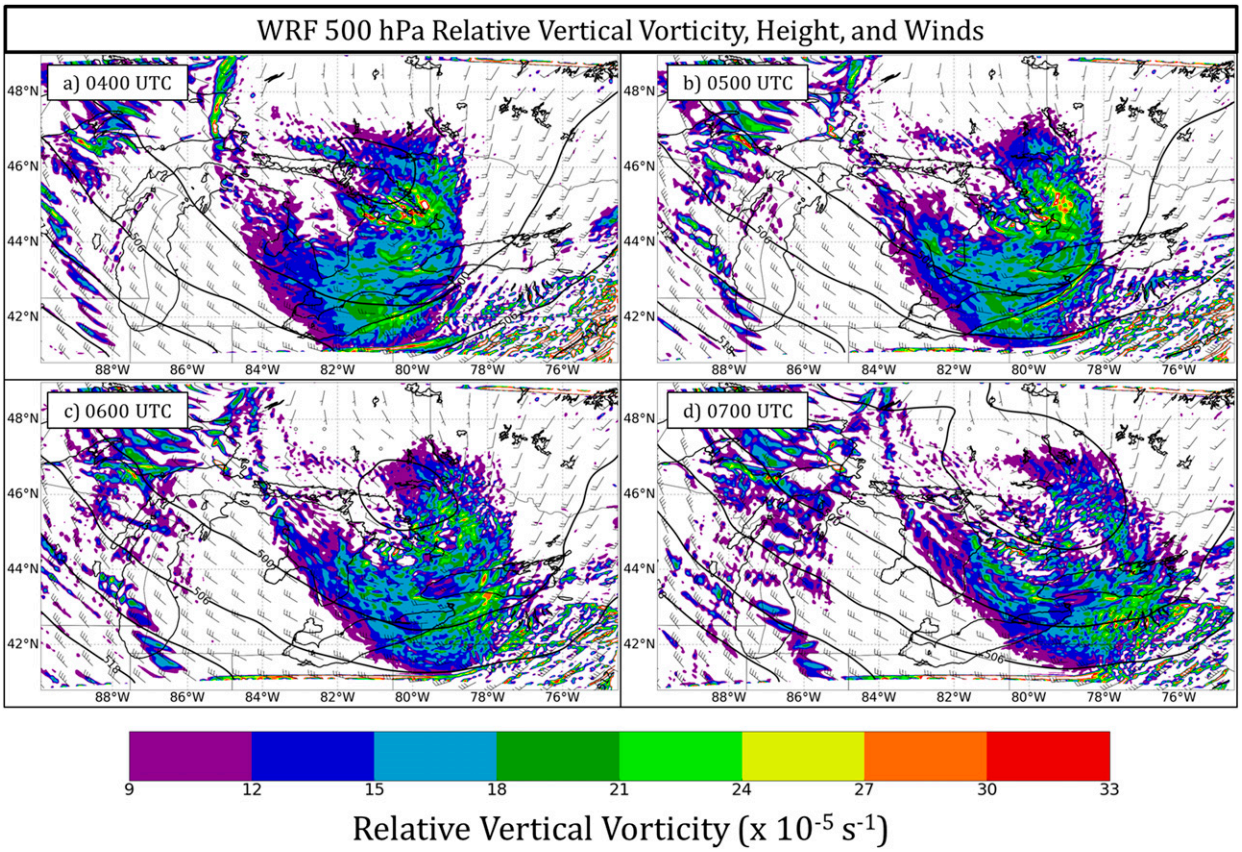

FIG. 16. 500-hPa winds ($\mathrm{m\,s^{-1}}$; half barb = 5 and full barb = $10\,\mathrm{m\,s^{-1}}$), geopotential height (contoured every 6 dam), and relative vertical vorticity ($\times 10^{-5}\,\mathrm{s^{-1}}$; color filled) from the WRF simulation (3-km domain) valid at (a) 0400, (b) 0500, (c) 0600, and (d) 0700 UTC 7 Jan 2014.

The quantity $(\partial^2\overline{u}/\partial y^2)(\overline{u}-\overline{u}_I)$ is plotted in Fig. 14 for the same time period (0630–0744 UTC). FIC is met between $y = 7$ and 16 km at 0630 UTC (Fig. 14a), which corresponds to the location of the shear zone and vortices, and also to where RIC is satisfied (cf. Figs. 13a and 14a). Each plot demonstrates that this more stringent instability criterion is also satisfied at the location of the shear zone and vortices, and where RIC is met, further supporting the hypothesis that HSI is the driving mechanism for the formation of the misovortices in this case. Without DOW radar operations, and subsequent DD analyses of incipient misovortex development, however, it is impossible to determine definitively the formation mechanism for the misovortices (e.g., Marquis et al. 2007).

Additional theories of misovortexgenesis include the introduction of vertical vorticity via tilting of the horizontal vorticity (e.g., Wilczak et al. 1992; Arnott et al. 2006). The lack of anticyclonic–cyclonic vortex couplets straddling the updrafts, however, implies that tilting is likely muted relative to the release of HSI and subsequent vortex stretching (Fig. 8; e.g., Wheatley and Trapp 2008). Figure 15 depicts the stretching term (at 500 m AGL) in the vertical vorticity tendency equation, which is defined here as

$$\frac{\partial\zeta}{\partial t} = -\mathbf{V}\cdot\nabla_H\zeta + \xi\left(\frac{\partial w}{\partial x}\right) + \eta\left(\frac{\partial w}{\partial y}\right) + \left(\frac{\partial v}{\partial x} - \frac{\partial u}{\partial y}\right)\frac{\partial w}{\partial z}, \quad (1)$$

where ζ is the vertical vorticity, $\mathbf{V} = (\mathbf{i}u + \mathbf{j}v + \mathbf{k}w)$ is the three-dimensional velocity vector, ξ is the x component of the horizontal vorticity, and η is the y component of the horizontal vorticity. The terms on the right-hand side of Eq. (1) represent (i) the horizontal advection of the relative vertical vorticity, (ii) the x component of the tilting of the horizontal vorticity, (iii) the y component of the tilting of the horizontal vorticity, and (iv) the stretching of the relative vertical vorticity. Typical magnitudes of stretching are generally between -1.0 and $4.0 \times 10^{-4}\,\mathrm{s^{-2}}$. This term is maximized within the cores of some of the vortices, where a maximum in vertical vorticity exists in the presence of upward vertical velocity (Figs. 8 and 15). A similar arrangement of

Unauthenticated | Downloaded 02/02/24 12:11 AM UTC

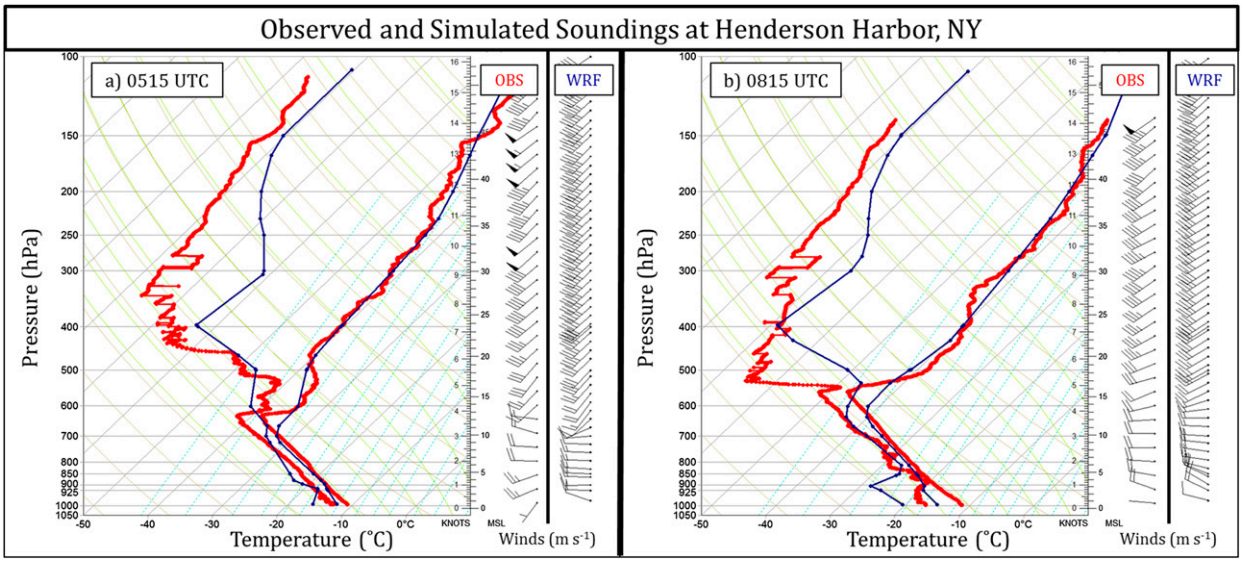

FIG. 17. Observed (red) and WRF-simulated (blue; 333-m domain) soundings at Henderson Harbor at (a) 0515 and (b) 0815 UTC 7 Jan 2014. Winds ($m\,s^{-1}$; half barb = 5, full barb = 10, and pennant = $50\,m\,s^{-1}$) for both soundings are plotted along the right side of each image.

stretching relative to the misovortices was noted in the simulations by Lee and Wilhelmson (1997). Additionally, Buban and Ziegler (2016) have also revealed that stretching dominates tilting in their simulations. Finally, tilting alone is unlikely to describe the local maxima in vertical vorticity near the surface (e.g., 500 m AGL) as vertical advection (within updrafts) results in the largest values of vorticity being displaced upward (e.g., Davies-Jones 1982a,b). Analyses of the tilting term from the vertical vorticity equation have been omitted owing to the aforementioned uncertainties in the DD-derived vertical velocity magnitudes.

The above analyses of the 7 January 2014 lake-effect band support the hypothesis proposed by Steiger et al. (2013) that the governing mechanism of misovortexgenesis in LLAP bands, at least in this particular case, is the release of HSI and subsequent strengthening via low-level vortex stretching.

5. WRF modeling perspective

a. Synoptic and mesoscale regime

A WRF simulation was performed of the 7 January 2014 lake-effect band to better elucidate details of features for which DD data are not available. The model configuration is detailed in section 2c, Fig. 2, and Table 2. Figure 16 portrays the evolution of the 500-hPa pattern between 0400 and 0700 UTC over the 3-km domain; the simulation depicts the approach of the short-wave trough reasonably well compared to the 13-km operational RAP model (cf. Figs. 3 and 16).

A comparison between observed and modeled soundings at Henderson Harbor, from the 333-m WRF domain at 0515 UTC, reveals that the modeled surface temperature and dewpoint temperature values are slightly too cold (Fig. 17), with a simulated surface temperature of approximately −12.5°C, whereas the observed surface temperature was approximately −11.5°C. Additionally, the simulation forecasts the top of the BL to be around 700 hPa, while it was actually around 625 hPa (Fig. 17a). This result is similar to the simulation of the LLAP case from the LOWS project, which also underestimated the depth of the BL (Reinking et al. 1993). At 0815 UTC, the simulation is too stable between 650 and 550 hPa (Fig. 17b) and too cold/dry at the surface; however, the observed and modeled soundings are qualitatively similar. In terms of the kinematic field, the simulation compares reasonably well with the observations, depicting BL wind speeds generally between 10 and 25 $m\,s^{-1}$. The simulated winds are a bit too northwesterly at 0515 UTC owing to a southward bias in the position of the simulated Lake Ontario band (more analysis on this below; Fig. 18). Despite the differences between the model and the observations, the simulation was more than adequate for the desired analyses regarding the misovortices.

A Georgian Bay band was connected with the Lake Ontario band between 0400 and 0800 UTC (Figs. 5 and 18). A comparison between the simulated composite reflectivity in the 1-km domain and the observed reflectivity from the King City radar reveals that the simulation accurately depicts the Georgian Bay band

Unauthenticated | Downloaded 02/02/24 12:11 AM UTC

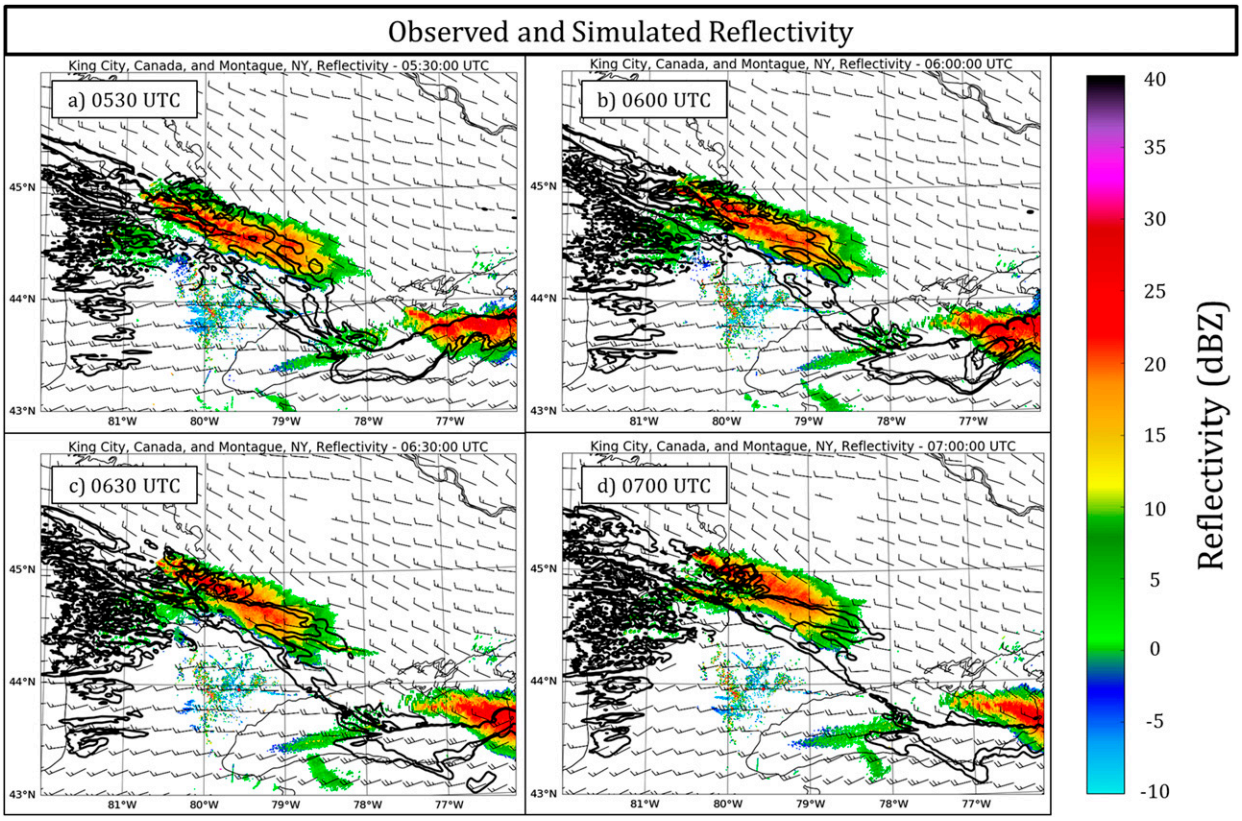

FIG. 18. Composite reflectivity (dBZ; 10- and 15-dBZ contours shown) and 500-m AGL horizontal winds (m s^{-1}; half barb = 5 and full barb = 10 m s^{-1}) from the WRF simulation (1-km domain) overlaid with KTYX and CWKR base reflectivity (dBZ; shaded) valid at (a) 0530, (b) 0600, (c) 0630, and (d) 0700 UTC 7 Jan 2014.

extending southeastward toward Lake Ontario, and the eventual progression of this upstream band northward (Fig. 18). A long fetch of relatively warmer 2-m air temperatures, generated by vertical sensible heat fluxes from the warmer waters of Georgian Bay, was advected southeastward toward Lake Ontario (not shown). This is consistent with previous studies that document that advection of heat and moisture favors the formation of heavier lake-effect bands over downstream lakes (e.g., Rodriguez et al. 2007). The simulated Lake Ontario band was approximately one bandwidth (20–30 km) too far south (Fig. 18), but was quite similar structurally to the observed band.

The simulation captured the string of misovortices that developed along the cyclonic horizontal shear zone (Fig. 19a). The shear zone appears to originate over western Lake Ontario; however, it can be traced farther westward, toward Georgian Bay. Over the western half of Lake Ontario, the cyclonic horizontal shear zone strengthens between 0400 and 0600 UTC, as vertical vorticity values along the shear zone increase from ~2 to >5 × 10^{-3} s^{-1} (Fig. 19). The shear zone eventually breaks into discrete patches of vertical vorticity after 0600 UTC across eastern Lake Ontario, forming misovortices [i.e., vortex sheet rollup; see also Juckes (1995)].

As the short-wave trough departs the region to the northeast and the midlevel short-wave ridge approaches, BL winds back from northwest (NW) to west (W), forcing the Georgian Bay band northward (Fig. 18). Eventually, the winds back sufficiently for the connection to be lost (Fig. 18d). The shear zone and associated string of misovortices over Lake Ontario may have been influenced by this connection, at least during a portion of this event. Coincident with the cessation of the connection, the string of misovortices vanishes from west to east, with only isolated instances of vortices throughout the remainder of the event (not shown).

b. *Vortex characteristics*

Dual-Doppler wind syntheses from this event reveal the presence of a string of misovortices, roughly evenly spaced within the band (Fig. 7; also see section 4). Figure 20 depicts a 40-min evolution of the vortices between 0750 and 0830 UTC, as this was when the

Unauthenticated | Downloaded 02/02/24 12:11 AM UTC

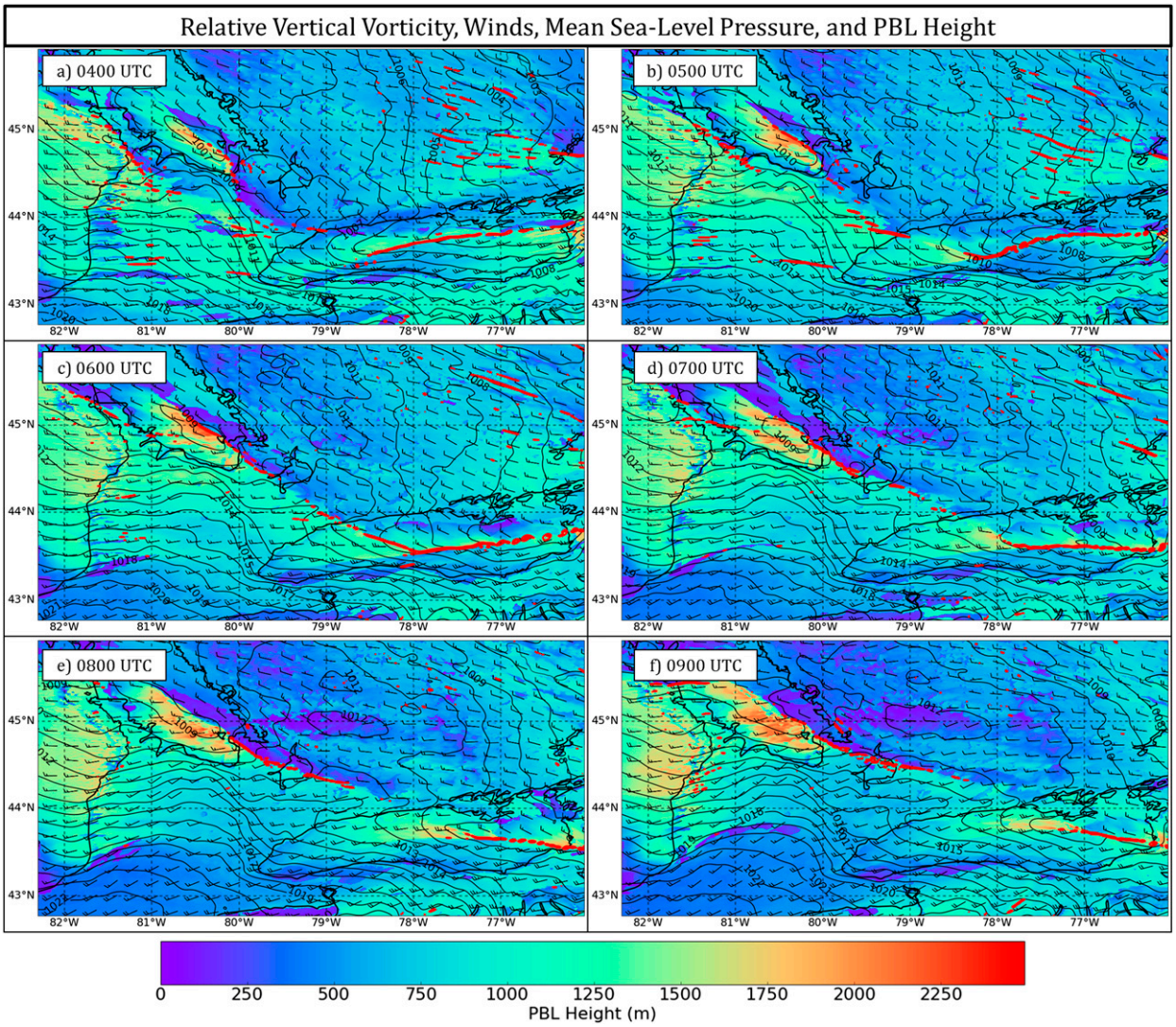

FIG. 19. 500-m AGL relative vertical vorticity (contoured in red from $2 \times 10^{-3}\,s^{-1}$ to 18×10^{-3} every $4 \times 10^{-3}\,s^{-1}$), planetary boundary layer height (m; shaded), mean sea level pressure (contoured in black every 1 hPa), and 500-m AGL horizontal winds ($m\,s^{-1}$; half barb = 5 and full barb = $10\,m\,s^{-1}$) from the WRF simulation (1-km domain) valid at (a) 0400, (b) 0500, (c) 0600, (d) 0700, (e) 0800, and (f) 0900 UTC 7 Jan 2014.

simulation most closely matched the observations. The simulated vortices are located along the northern side of the band, near a sharp north-south horizontal reflectivity gradient (Fig. 20), similar to the DD analyses (Fig. 7). Vortices D–J were tracked between 0750 and 0820 UTC and exhibit an east-southeastward motion, with an average propagation speed of $26.5\,m\,s^{-1}$ (approximately $7.5\,m\,s^{-1}$ faster than the observed vortices). These vortices also appear to move with the mean wind within the vortex-bearing layer (0–2 km AGL). The average horizontal spacing between the vortices during this time period was approximately 6.5 km (nearly identical to the DD-analyzed vortex spacing of 6.6 km). The vortices are persistent and can be tracked for greater than 40 min as they propagate along the wind shift. Unlike in the DD analyses, however, there is at least one vortex interaction during this period. Vortex I, which at 0800 UTC is slightly stronger and larger than vortex H, merges with vortex H by 0815 UTC (Figs. 20c,d; merged vortex labeled HI). The two vortices appear to rotate cyclonically about one another between 0800 and 0815 UTC, similar to the Fujiwhara effect (Fujiwhara 1923, 1931). With a few exceptions in the WRF simulation, the vortices, both observed and simulated, remain discrete as they propagate eastward along the shear zone.

Since DD data are not available east of Lake Ontario, the WRF simulation was useful in determining if the simulated vortices could persist inland (e.g., Fig. 21).

Unauthenticated | Downloaded 02/02/24 12:11 AM UTC

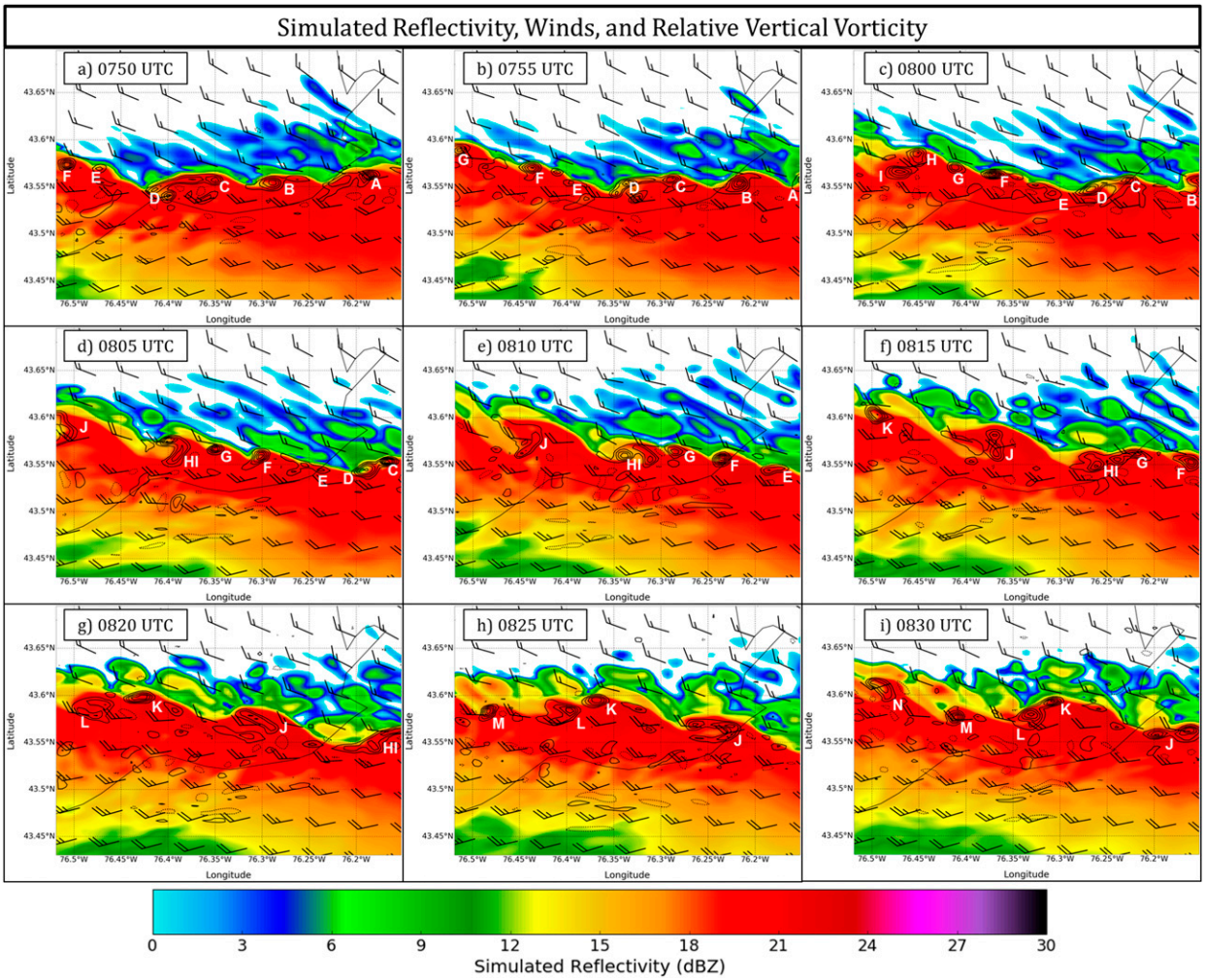

FIG. 20. 500-m AGL relative vertical vorticity (contoured every $0.5 \times 10^{-2}\,s^{-1}$ starting at $-5.5 \times 10^{-2}\,s^{-1}$; solid = positive and dashed = negative), composite reflectivity (dBZ; shaded), and horizontal winds ($m\,s^{-1}$; half barb = 5 and full barb = $10\,m\,s^{-1}$) from the WRF simulation (333-m domain) valid at (a) 0750, (b) 0755, (c) 0800, (d) 0805, (e) 0810, (f) 0815, (g) 0820, (h) 0825, and (i) 0830 UTC 7 Jan 2014. Each misovortex is labeled with a capital letter between A and N.

The WRF analyses indicate that the vortices do not persist for more than 15 km inland (not shown), likely because the lack of a low-level buoyancy source (i.e., relatively warm lake waters) precludes low-level vortex stretching from occurring inland as the surface roughness and viscous dissipation increase (e.g., see terrain map in Fig. 1). This agrees with the findings of Minder et al. (2015), who describe the convective-to-stratiform transition of the lake-effect convection as it penetrates inland. A study by Inoue et al. (2011), which analyzed misovortices within sea-effect snows near the Sea of Japan, also found that the misovortices weakened upon landfall owing to an increase in surface roughness, which in turn increased the frictional dissipation rate [see also Dessens (1972) and Leslie (1977)]. Hence, while the vortices may be quasi–steady state over the lake, once they move inland and are removed from the warmer lake waters, they rapidly dissipate.

A closer examination of the simulated misovortices reveals additional similarities to warm-season vortices documented in previous studies (e.g., Marquis et al. 2007) and to the aforementioned DD analyses (section 4). Figure 22 depicts the 500 m AGL vertical velocity and vertical vorticity from the 333-m domain between 0750 and 0830 UTC. Updraft magnitudes at 500 m AGL from the simulation range between 2 and $5\,m\,s^{-1}$, and the vertical vorticity within the misovortices is between 2 and $5 \times 10^{-2}\,s^{-1}$ (Fig. 22). These values are similar (yet slightly larger) to those from the DD analyses (see section 4a), which depict 500 m AGL vertical velocity and vertical vorticity values between 1–3 $m\,s^{-1}$ and 1–3 $\times\ 10^{-2}\,s^{-1}$, respectively (Fig. 8), despite the slight difference in

Unauthenticated | Downloaded 02/02/24 12:11 AM UTC

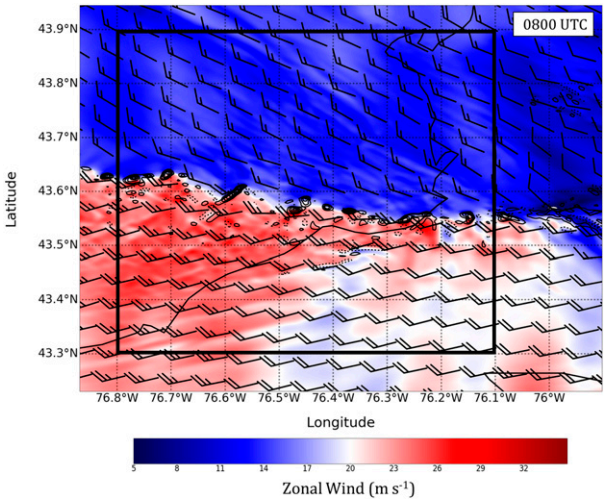

FIG. 21. 500-m AGL relative vertical vorticity (contoured every $0.5 \times 10^{-2}\,\mathrm{s}^{-1}$ starting at $-5.5 \times 10^{-2}\,\mathrm{s}^{-1}$; solid = positive and dashed = negative) and horizontal zonal wind ($\mathrm{m\,s}^{-1}$; shaded) from the WRF simulation (333-m domain) valid at 0800 UTC 7 Jan 2014. The black box denotes the domain where the HSI criteria are analyzed in Figs. 24 and 25.

horizontal resolution. The vortices are not typically collocated with updraft maxima, as in the DD analyses (Fig. 8). Some of the stronger simulated vortices exhibit weak downdrafts ($\sim 1\,\mathrm{m\,s}^{-1}$) near their cores (e.g., Fig. 22i; vortex L), also as in the DD analyses. It is possible that the rotation of a misovortex induces a downward-directed perturbation pressure gradient force owing to the largest values of vertical vorticity being located near the surface. This hypothesis was suggested by Mueller and Carbone (1987) to describe downdrafts within misovortices along a thunderstorm outflow boundary and has also been noted in idealized simulations of misovortices (e.g., Buban and Ziegler 2016).

A north–south vertical cross section, taken through one of the simulated misovortices at 0800 UTC (orange line in Fig. 22c; vortex G), is depicted in Fig. 23. The misovortex, which has a maximum vertical vorticity value of $\sim 2 \times 10^{-2}\,\mathrm{s}^{-1}$ between the surface and 0.5 km AGL, weakens rapidly with height above 1 km AGL. Similar to the vertical cross section from the DD analysis (Fig. 10), the simulated vortex tilts toward the south with height owing to a stronger northerly wind component aloft (Fig. 23). The relative positions of the updraft and vortex are also similar to those in the DD-analyzed vertical cross section (Fig. 10), with the largest vertical velocities (3–5 $\mathrm{m\,s}^{-1}$) displaced slightly north of (and above) the vortex. Finally, the greatest upward vertical motion is juxtaposed with a sharp reflectivity gradient, which results from hydrometeor lofting, horizontal advection, and subsequent fall out, leading to enhanced reflectivity just south of the updraft (e.g., Fig. 20).

c. *Horizontal shearing instability*

The preceding DD analyses support that the release of HSI is the leading cause of misovortexgenesis (see section 4b and Steiger et al. 2013), with further strengthening via vortex stretching beneath updrafts. Both RIC and FIC, which were examined from the DD wind synthesis in section 4b, are analyzed below from the 333-m WRF simulation.

Figure 24 depicts RIC every 15 min between 0730 and 0845 UTC. This criterion is met at each analysis time during this period, with sign changes of $\partial^2\overline{u}/\partial y^2$, collocated with the shear zone and vortices (denoted by the red dashed lines in Fig. 24). Additionally, Fjørtoft's more stringent instability criterion is also satisfied at these locations (Fig. 25). Hence, both the DD and WRF analyses support the hypothesis that HSI is the primary formation mechanism of the misovortices within this band.

Tilting and stretching terms [see Eq. (1)] were calculated from the WRF output to reveal the relative contributions to misovortexgenesis (Figs. 26 and 27). Regions of enhanced tilting are generally located along the periphery of the vortices where there is a sharp gradient in vertical velocity (Fig. 26), with enhanced values of stretching within the cores of the vortices (Fig. 27). Furthermore, the stretching term (values from -0.50 to $3.00 \times 10^{-4}\,\mathrm{s}^{-2}$) is much larger than the tilting term (values from -0.50 to $0.50 \times 10^{-4}\,\mathrm{s}^{-2}$). This supports the hypothesis that tilting is of less importance than the release of HSI and subsequent stretching in the development of the misovortices within this band.

d. *Cyclonic horizontal shear zone over Lake Ontario*

The model analyses in section 5a depict a cyclonic horizontal shear zone that extends the length of Lake Ontario (Fig. 19). To explain the origin of this shear zone, an analysis of the background synoptic regime is necessary. A stronger pressure gradient (and hence faster westerly winds) is located across southern Lake Ontario and a weaker pressure gradient (and slower winds) is located across northern Lake Ontario between 0400 and 0900 UTC (Fig. 19). This lake-enhanced pressure trough propagates southward initially, before lifting back northward between 0700 and 0900 UTC (Figs. 19d–f). Steiger et al. (2013) postulate that an enhanced mesoscale pressure gradient across southern Lake Ontario might explain why faster westerly winds are often observed on the south side of west-to-east-oriented lake-effect bands, resulting in a cyclonic horizontal shear zone (and subsequent cyclonic vortices). For west-to-east-oriented LLAP bands, the synoptic-scale BL winds

Unauthenticated | Downloaded 02/02/24 12:11 AM UTC

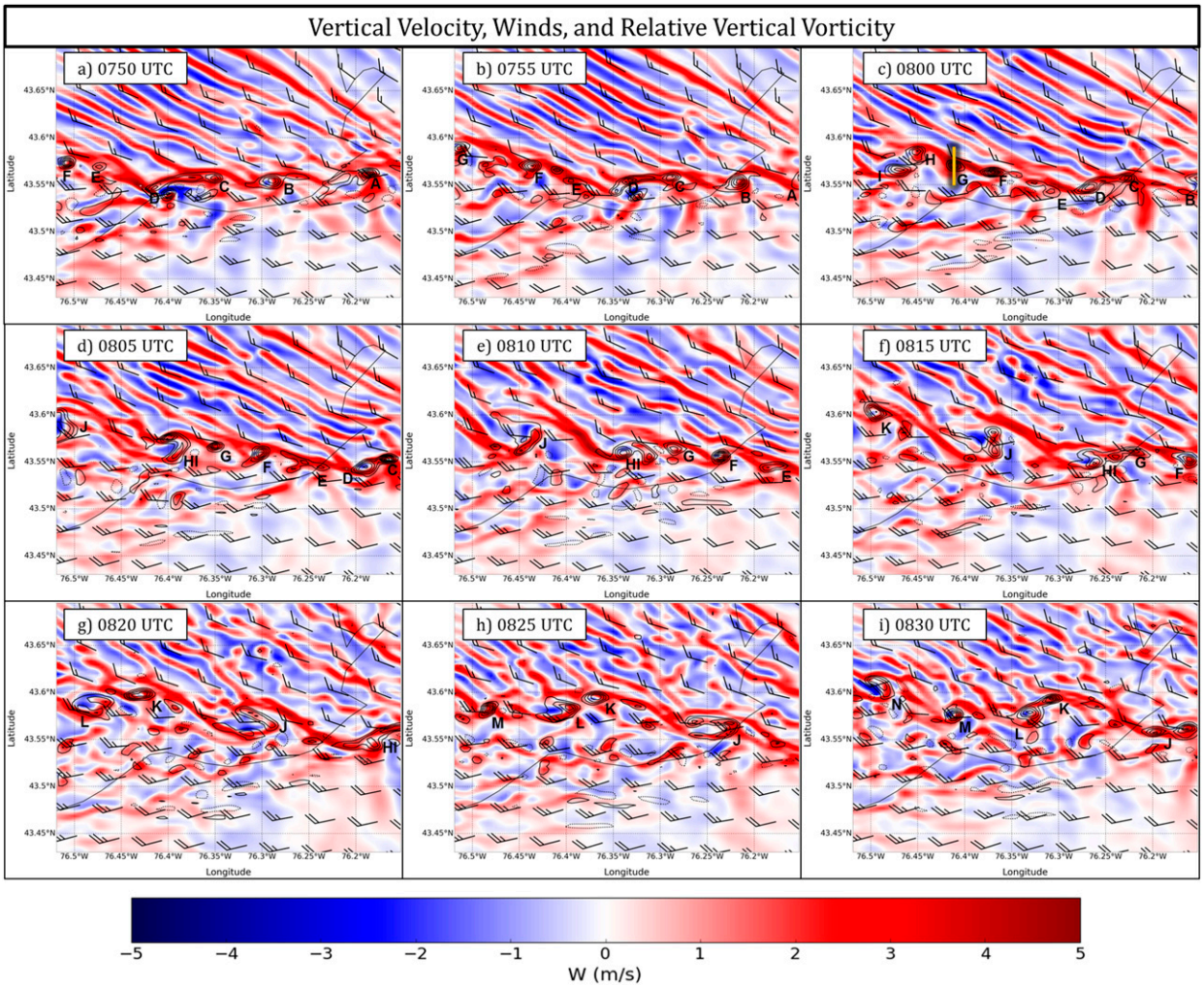

FIG. 22. 500-m AGL relative vertical vorticity (contoured every $0.5 \times 10^{-2}\,\mathrm{s}^{-1}$ starting at $-5.5 \times 10^{-2}\,\mathrm{s}^{-1}$; solid = positive and dashed = negative), vertical velocity ($\mathrm{m\,s}^{-1}$; color filled), and horizontal winds ($\mathrm{m\,s}^{-1}$; half barb = 5 and full barb = $10\,\mathrm{m\,s}^{-1}$) from the WRF simulation (333-m domain) valid at (a) 0750, (b) 0755, (c) 0800, (d) 0805, (e) 0810, (f) 0815, (g) 0820, (h) 0825, and (i) 0830 UTC 7 Jan 2014. Each misovortex is labeled with a capital letter between A and N. The orange line in (c) denotes the south-to-north vertical cross section displayed in Fig. 23.

are roughly westerly, meaning that lower pressures must exist north of the lake with higher pressures south of the lake. In time, as sensible heat from the lake surface is advected vertically, an elongated mesoscale area of low pressure develops underneath the band. The lower surface pressure over the lake relaxes the horizontal pressure gradient across the northern portion of the lake while enhancing it across the southern portion of the lake (see pressure field in Fig. 19). Thus, faster westerly BL flow is favored on the southern side of the lake near these west-to-east-oriented LLAP bands, fostering the maintenance of a cyclonic horizontal shear zone within the band, along which cyclonic misovortices may develop and propagate. Unfortunately, no surface weather data were available over the lake during this event, owing to the extreme winter weather conditions, to provide observational evidence for this hypothesis; however, the WRF simulation supports this claim.

The importance of the interaction between the upstream vortex sheet from Georgian Bay and that over Lake Ontario is still an area of active research. A comparison between the 1-km domain from the WRF simulation presented above and another where the upstream lakes were removed reveals that the cyclonic horizontal shear zone still develops over Lake Ontario, albeit a bit weaker (not shown). Additional analyses of these simulations are in progress and are planned for a future publication.

Unauthenticated | Downloaded 02/02/24 12:11 AM UTC

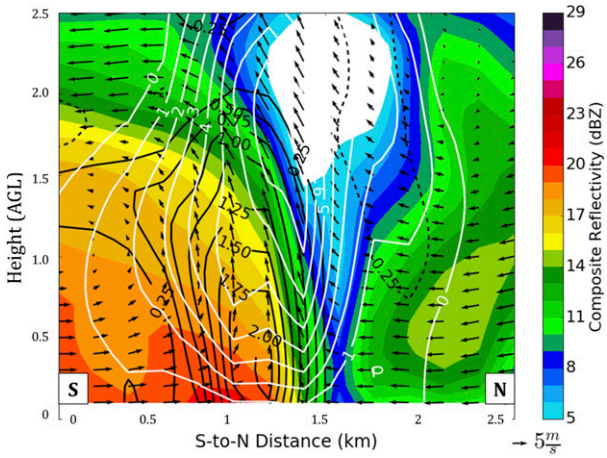

FIG. 23. South-to-north vertical cross section along the orange line through vortex G in Fig. 22c at 0800 UTC. Composite reflectivity (dBZ; color filled), vertical velocity (only positive values plotted; contoured in white every 1 m s^{-1} starting at 0 m s^{-1}), vertical vorticity (contoured every 0.25×10^{-2} s^{-1} starting at -5.5×10^{-2} s^{-1}; solid = positive and dashed = negative; zero contour suppressed), and wind vectors (v and w components only; m s^{-1}) from the WRF simulation (333-m domain).

6. Summary and conclusions

The OWLeS project (Kristovich et al. 2017) took place during the winter of 2013/14. The main goal of this project was to gather in situ data within lake-effect snowstorms over and downwind of Lake Ontario. On 7 January 2014, during an outbreak of extremely cold temperatures (e.g., 850 hPa temperatures around −25°C), a long-duration (>20 h) LLAP band developed over Lake Ontario and exhibited numerous small-scale vortices. Multiple Doppler radars were deployed along the Lake Ontario shoreline during this event, which allowed for three-dimensional dual-Doppler wind syntheses to be constructed.

A string of misovortices occurred between 0400 and 0800 UTC, followed by a regime consisting of only isolated misovortices. Individual vortices were tracked for well over 30 min, and vortices generally did not merge or otherwise interact with other vortices. The vortices developed along a cyclonic horizontal shear zone located near the northern edge of the band, which corresponded to the ascending branch of a transverse secondary circulation pattern. This circulation reached an altitude of around 2 km AGL. Vertical velocities at 500 m AGL were typically between 1 and 3 m s^{-1}, although isolated, more vigorous updrafts were noted in the DD analyses. This line of updrafts was located near a sharp north–south horizontal gradient in reflectivity and was attributable to hydrometeor lofting and subsequent horizontal advection aloft and fallout.

The convergence–divergence pattern near the vortices resembled that documented in previous studies, with regions of localized convergence NE and SW of the vortices and near-zero convergence (or sometimes weak divergence) within their cores. Vertical cross sections through the vortices reveal that their circulation patterns were most intense around 1 km AGL and weakened with height above this level. The vortices tilted southward with height, owing to a stronger northerly

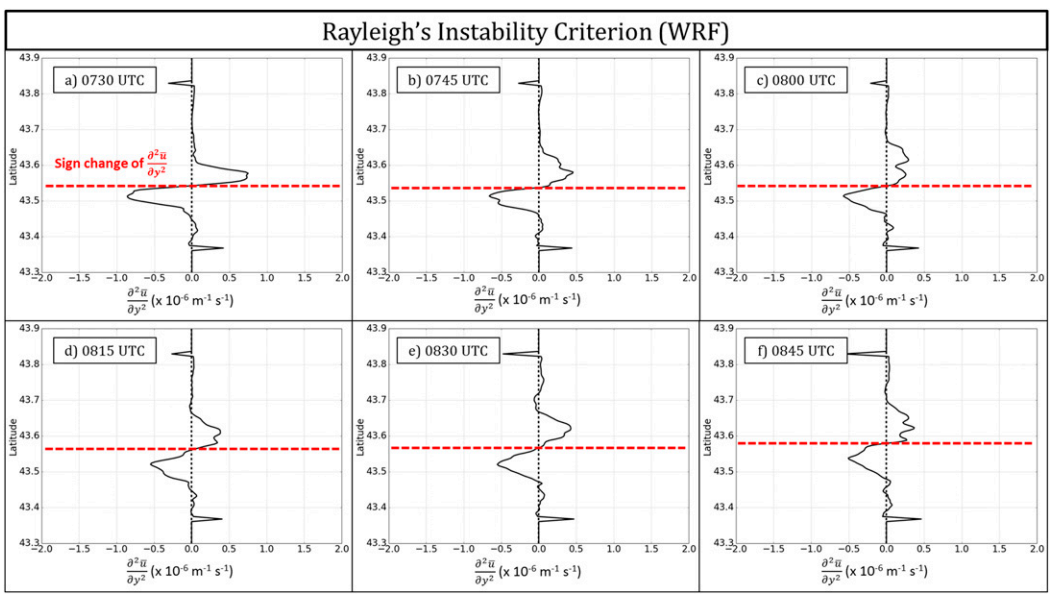

FIG. 24. The quantity $\partial^2\overline{u}/\partial y^2$ ($\times 10^{-6}$ m^{-1} s^{-1}) vs latitude (°) from the WRF simulation (333-m grid) at 500 m AGL valid at (a) 0730, (b) 0745, (c) 0800, (d) 0815, (e) 0830, and (f) 0845 UTC 7 Jan 2014. The red dashed lines denote the location where RIC is satisfied.

Unauthenticated | Downloaded 02/02/24 12:11 AM UTC

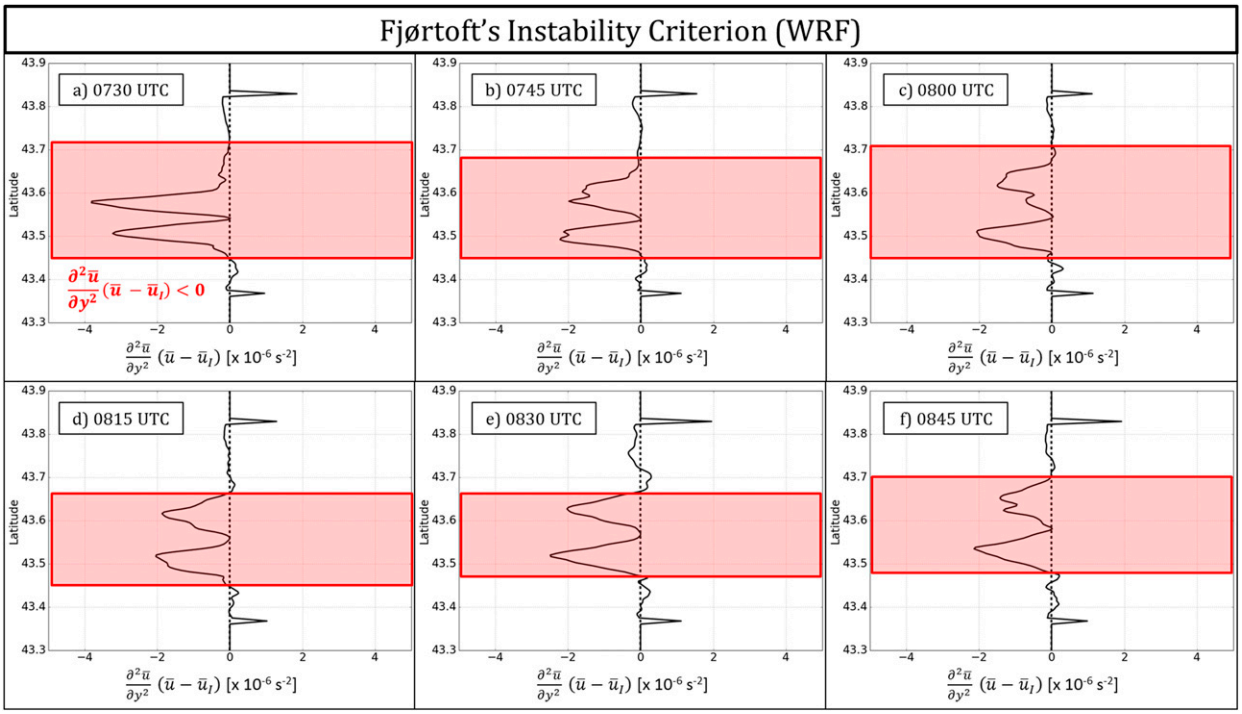

FIG. 25. The quantity $(\partial^2\overline{u}/\partial y^2)(\overline{u} - \overline{u}_l)$ ($\times 10^{-6}\,\mathrm{s}^{-2}$) vs latitude (°) from the WRF simulation (333-m grid) at 500 m AGL valid at (a) 0730, (b) 0745, (c) 0800, (d) 0815, (e) 0830, and (f) 0845 UTC 7 Jan 2014. The red shaded rectangles indicate where FIC is satisfied.

wind component near band top. There was generally some degree of overlap between the updrafts and the vortices, which aided in vortex strengthening and maintenance via stretching, but also instances of vortices that weakened within regions of downward vertical motion.

A high-resolution WRF simulation was conducted, which also depicts misovortices developing along the cyclonic horizontal shear zone, as in the DD analyses. The relative intensity, along with the spacing and depth of the simulated vortices, compares remarkably well with the observed vortices. The simulated vortices are also characterized by regions of convergence and upward vertical motion generally NE and SW of their centers, with near-zero vertical motion (or sometimes weak downdrafts) within their cores. Vertical cross sections through the simulated vortices depict the largest values of vertical vorticity between the surface and 1 km AGL, along with a southward tilt with height, similar to in the DD-derived vertical cross sections.

The leading hypothesis for the development of the misovortices is the release of HSI. Two instability criteria (Rayleigh's and Fjørtoft's criteria for HSI) were calculated and analyzed, from both the DD wind synthesis and the WRF simulation, to investigate whether HSI was the primary mechanism of misovortexgenesis in this case. Both instability criteria are satisfied at multiple times along the shear zone in both the observations and the simulation, strongly supporting the HSI hypothesis. Furthermore, the lack of anticyclonic–cyclonic vortex couplets throughout most of the event reveals that the competing hypothesis that tilting of vertical wind shear–induced horizontal vorticity into the vertical driving misovortexgenesis is likely muted. Finally, the nearly equally spaced, like-signed (only cyclonic) vortices along the horizontal shear zone are another indication that the release of HSI was responsible for their initiation (e.g., Wheatley and Trapp 2008). Once the vortices reach the eastern shore of Lake Ontario, they rapidly weaken as increasing viscous dissipation, owing to increasing surface roughness, overwhelms the decreasing vortex stretching as the vortices propagate away from the relatively warm lake waters and low-level updrafts weaken.

The WRF simulation depicts a cyclonic horizontal shear zone, emanating over western Lake Ontario. This vortex sheet is contiguous across northwestern Lake Ontario but breaks into discrete vortices over eastern Lake Ontario. The associated wind shift eventually propagates northward in tandem with backing BL winds attributable to an approaching midlevel short-wave ridge, marking the end of the string of misovortices.

The shear zone accompanying this LLAP band is exclusively cyclonic across Lake Ontario. Falling surface pressures due to low-level heating over Lake Ontario likely aided in the development of a near-surface

Unauthenticated | Downloaded 02/02/24 12:11 AM UTC

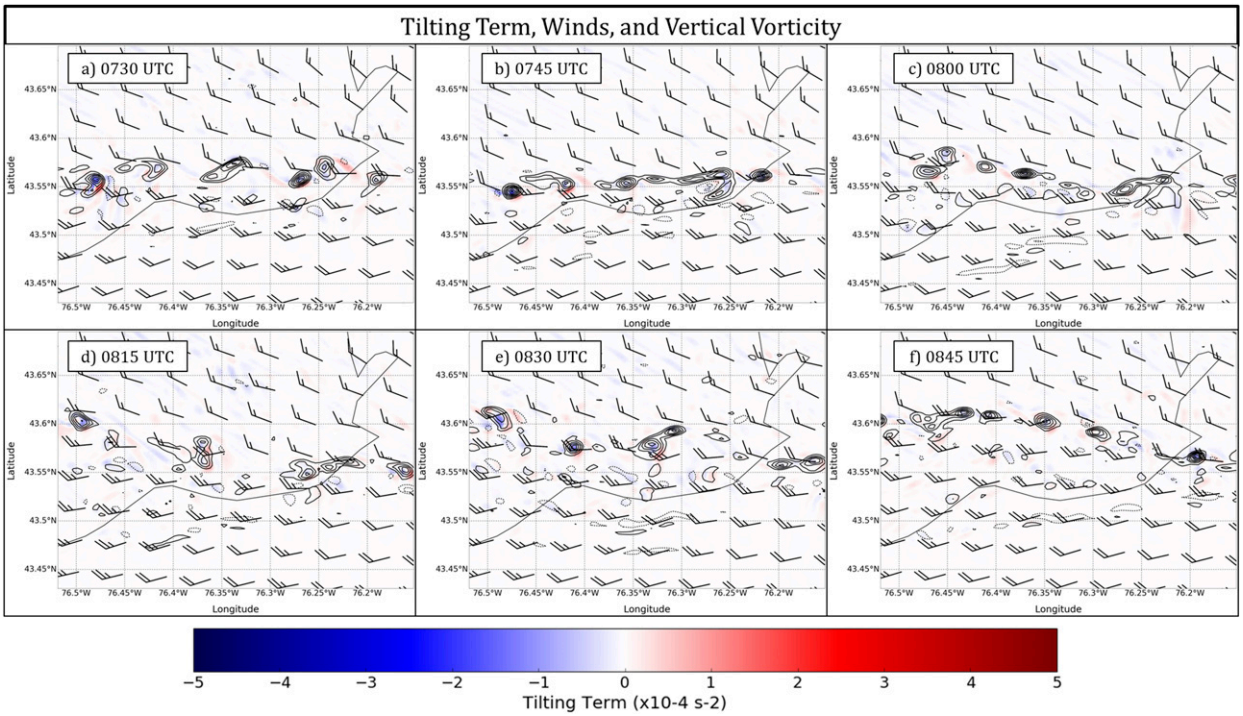

FIG. 26. Tilting term ($\times 10^{-4}\,\mathrm{s}^{-2}$; shaded) from the WRF simulation (333-m domain) at 500 m AGL. Horizontal winds ($\mathrm{m\,s}^{-1}$; half barb = 5 and full barb = $10\,\mathrm{m\,s}^{-1}$) and relative vertical vorticity (contoured every $0.5 \times 10^{-2}\,\mathrm{s}^{-1}$ starting at $-5.5 \times 10^{-2}\,\mathrm{s}^{-1}$; solid = positive and dashed = negative) valid at (a) 0730, (b) 0745, (c) 0800, (d) 0815, (e) 0830, and (f) 0845 UTC 7 Jan 2014.

mesolow, increasing convergence into the band. With higher pressures south of the lake and lower pressures north, faster westerly winds developed over southern Lake Ontario, with slower westerly winds to the north, resulting in a cyclonic horizontal shear zone along which the vortices developed and propagated. Cyclonic horizontal shear zones are thought to be intrinsic to west-to-east-oriented LLAP bands, as the aforementioned synoptic-scale pattern is necessary for mean westerly flow along the major axis of Lake Ontario (section 5d). The hypothesis for the formation of the upstream shear zone emanating from Georgian Bay, and its relative importance in the shear zone and misovortices over Lake Ontario, is more unclear and future model sensitivity studies are planned to answer this question.

While the vortices in this study resemble those from previous studies (e.g., Marquis et al. 2007 and others), inherent differences in ambient environments remain regarding details such as surface roughness, buoyancy gradients, and baroclinicity. Previous studies have analyzed vortices in lower latitudes and during the spring months; hence, formation and maintenance mechanisms between lake-effect vortices and other vortices likely exhibit a degree of dissimilarity. More research is warranted in the field of lake-effect vortices, as other cases have featured mesovortices that are qualitatively similar to supercell thunderstorms (Steiger et al. 2013) and, hence, may form through a different mechanism (e.g., tilting of horizontal vorticity) than the smaller-scale misovortices discussed herein (release of HSI). These lake-effect misovortices, however, are dynamically different than the vortices examined in studies by Forbes and Merritt (1984), Grim et al. (2004), and Laird et al. (2001).

The continual push to understand the mechanisms that govern the formation, maintenance, and demise of these LLAP bands and associated convergence boundaries/shear zones, misovortices, and lake-to-lake connections will likely be particularly useful to add to the scope of lake-effect research. Additional cases of strings of misovortices within LLAP bands over Lake Ontario during the OWLeS project will be examined in the future, also using three-dimensional DD wind syntheses and high-resolution model simulations to compare and contrast vortex characteristics and formation mechanisms. Cases in which the cyclonic horizontal shear zone is along the southern edge of the LLAP band, or within the center of the band, will also be evaluated.

Acknowledgments. The authors thank the many participants (too numerous to mention) in the OWLeS Project who collected data in often formidable and adverse weather conditions. Many thanks go to Rachel Humphries

Unauthenticated | Downloaded 02/02/24 12:11 AM UTC

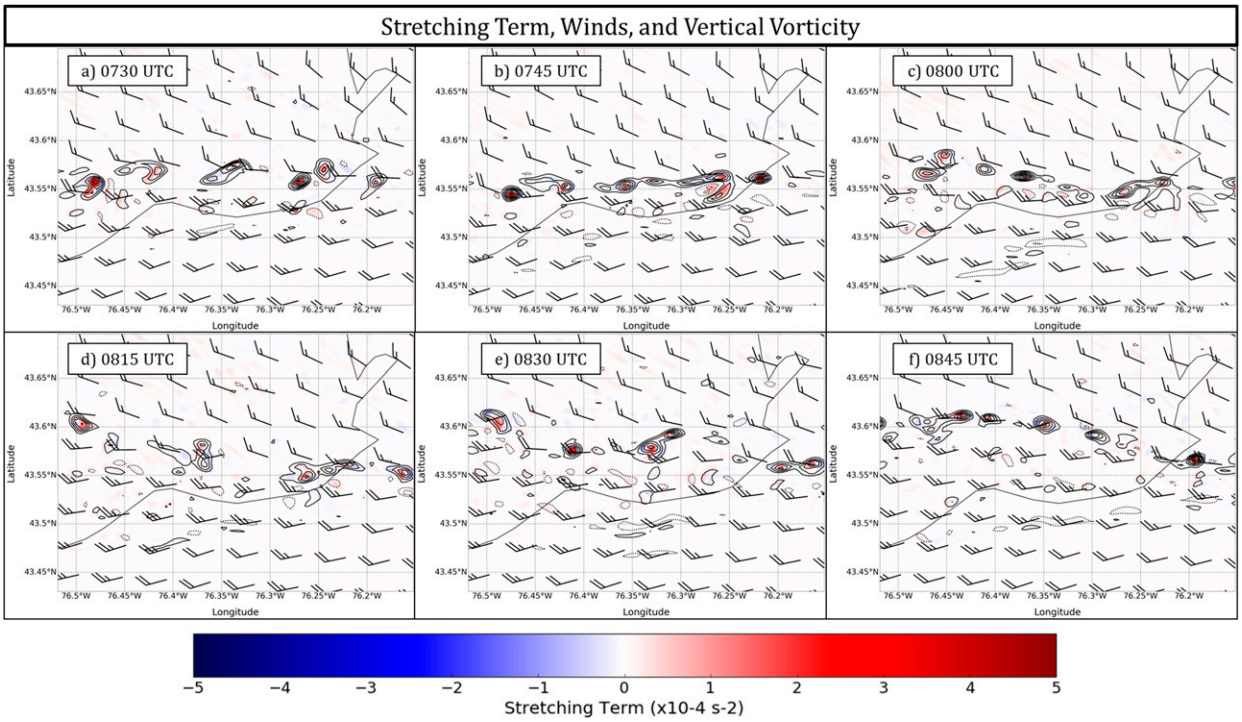

FIG. 27. Stretching term ($\times 10^{-4}\,\mathrm{s}^{-2}$; shaded) from the WRF simulation (333-m domain) at 500 m AGL. Horizontal winds ($\mathrm{m\,s}^{-1}$; half barb = 5 and full barb = $10\,\mathrm{m\,s}^{-1}$) and relative vertical vorticity (contoured every $0.5 \times 10^{-2}\,\mathrm{s}^{-1}$ starting at $-5.5 \times 10^{-2}\,\mathrm{s}^{-1}$; solid = positive and dashed = negative) valid at (a) 0730, (b) 0745, (c) 0800, (d) 0815, (e) 0830, and (f) 0845 UTC 7 Jan 2014.

and Paul Robinson of the Center for Severe Weather Research (CSWR), who helped with postprocessing of the Doppler-on-Wheels (DOW) data; Professor Robert Ballentine (retired; SUNY, Oswego), Tyler Kranz (The University of Arizona), Dillon Ulrich (University of Utah), and Andrew Janiszeski (University of Illinois at Urbana–Champaign; UIUC), along with Dr. Brian Jewett and Chuan-Chieh Chang of UIUC for their assistance with the WRF Model simulation; Benjamin Vega-Westhoff, Chen Wang, Kenneth Patten, and David Wojtowicz (UIUC) for computing assistance; and Professors Robert Rauber and Robert Trapp (UIUC) and Janice Mulholland for their helpful comments improving this manuscript. The authors would also like to thank editor Professor Todd Lane and three anonymous reviewers for improving this manuscript. Support for this work was made possible by National Science Foundation Grant AGS 12-59257.

REFERENCES

Arnott, N., Y. Richardson, J. Wurman, and E. N. Rasmussen, 2006: Relationship between a weakening cold front, misocyclones, and cloud development on 10 June 2002 during IHOP. *Mon. Wea. Rev.*, **134**, 311–335, doi:10.1175/MWR3065.1.

Barnes, S. L., 1964: A technique for maximizing details in numerical weather map analysis. *J. Appl. Meteor.*, **3**, 396–409, doi:10.1175/1520-0450(1964)003<0396:ATFMDI>2.0.CO;2.

Bell, M. M., W. C. Lee, C. A. Wolff, and H. Cai, 2013: A Solo-based automated quality control algorithm for airborne tail Doppler radar data. *J. Appl. Meteor. Climatol.*, **52**, 2509–2528, doi:10.1175/JAMC-D-12-0283.1.

Buban, M. S., and C. L. Ziegler, 2016: The formation of small-scale atmospheric vortices via baroclinic horizontal shearing instability. *J. Atmos. Sci.*, **73**, 2085–2104, doi:10.1175/JAS-D-14-0385.1.

——, ——, E. N. Rasmussen, and Y. R. Richardson, 2007: The dryline on 22 May 2002 during IHOP: Ground-radar and in situ data analysis of the dryline and boundary layer evolution. *Mon. Wea. Rev.*, **135**, 2473–2505, doi:10.1175/MWR3453.1.

Byrd, G. P., R. A. Anstett, J. E. Heim, and D. M. Usinski, 1991: Mobile sounding observations of lake-effect snow bands in western and central New York. *Mon. Wea. Rev.*, **119**, 2323–2332, doi:10.1175/1520-0493(1991)119<2323:MSOOLE>2.0.CO;2.

Campbell, P. C., B. Geerts, and P. T. Bergmaier, 2014: A dryline in southeast Wyoming. Part I: Multiscale analysis using observations and modeling on 22 June 2010. *Mon. Wea. Rev.*, **142**, 268–289, doi:10.1175/MWR-D-13-00049.1.

Davies-Jones, R. P., 1982a: A new look at the vorticity equation with application to tornadogenesis. Preprints, *12th Conf. on Severe Local Storms*, San Antonio, TX, Amer. Meteor. Soc., 249–252.

——, 1982b: Observational and theoretical aspects of tornadogenesis. *Intense Atmospheric Vortices*, L. Bengtsson and J. Lighthill, Eds., Springer-Verlag, 175–189.

Dessens, J., 1972: Influence of ground roughness on tornadoes: A laboratory simulation. *J. Appl. Meteor.*, **11**, 72–75, doi:10.1175/1520-0450(1972)011<0072:IOGROT>2.0.CO;2.

Unauthenticated | Downloaded 02/02/24 12:11 AM UTC

Dixon, M., and J. C. Hubbert, 2012: The separation of noise and signal components in Doppler RADAR returns. Preprints, *Seventh European Conf. on Radar in Meteorology and Hydrology*, Toulouse, France, Météo-France, SP-078. [Available online at https://www.eol.ucar.edu/projects/dynamo/spol/references/Separation_Noise_Signal.Dixon.ext_abs2012.pdf.]

Fabry, F., 2015: *Radar Meteorology: Principles and Practice.* Cambridge University Press, 256 pp.

Fjørtoft, R., 1950: Application of integral theorems in deriving criteria of stability for laminar flows and for the baroclinic circular vortex. *Geofys. Publ.*, **17** (6), 1–52.

Forbes, G. S., and J. H. Merritt, 1984: Mesoscale vortices over the Great Lakes in wintertime. *Mon. Wea. Rev.*, **112**, 377–381, doi:10.1175/1520-0493(1984)112<0377:MVOTGL>2.0.CO;2.

Fujita, T. T., 1981: Tornadoes and downbursts in the context of generalized planetary scales. *J. Atmos. Sci.*, **38**, 1511–1534, doi:10.1175/1520-0469(1981)038<1511:TADITC>2.0.CO;2.

Fujiwhara, S., 1923: On the growth and decay of vortical systems. *Quart. J. Roy. Meteor. Soc.*, **49**, 75–104, doi:10.1002/qj.49704920602.

——, 1931: Short note on the behavior of two vortices. *Proc. Phys.-Math. Soc. Japan*, Ser. 3, **13**, 106–110.

Grim, J. A., N. F. Laird, and D. A. R. Kristovich, 2004: Mesoscale vortices embedded within a lake-effect shoreline band. *Mon. Wea. Rev.*, **132**, 2269–2274, doi:10.1175/1520-0493(2004)132<2269:MVEWAL>2.0.CO;2.

Iacono, M. J., J. S. Delamere, E. J. Mlawer, M. W. Shephard, S. A. Clough, and W. D. Collins, 2008: Radiative forcing by long-lived greenhouse gases: Calculations with the AER radiative transfer models. *J. Geophys. Res.*, **113**, D13103, doi:10.1029/2008JD009944.

Inoue, H. Y., and Coauthors, 2011: Finescale Doppler radar observation of a tornado and low-level misocyclones within a winter storm in the Japan Sea coastal region. *Mon. Wea. Rev.*, **139**, 351–369, doi:10.1175/2010MWR3247.1.

Jiménez, P. A., J. Dudhia, J. F. González-Rouco, J. Navarro, J. P. Montávez, and E. García-Bustamante, 2012: A revised scheme for the WRF surface layer formulation. *Mon. Wea. Rev.*, **140**, 898–918, doi:10.1175/MWR-D-11-00056.1.

Juckes, M., 1995: Instability of surface and upper-tropospheric shear lines. *J. Atmos. Sci.*, **52**, 3247–3262, doi:10.1175/1520-0469(1995)052<3247:IOSAUT>2.0.CO;2.

Karan, H., and K. Knupp, 2006: Mobile Integrated Profiler System (MIPS) observations of low-level convergent boundaries during IHOP. *Mon. Wea. Rev.*, **134**, 92–112, doi:10.1175/MWR3058.1.

Kawashima, M., and Y. Fujiyoshi, 2005: Shear instability wave along a snowband: Instability structure, evolution, and energetics derived from dual-Doppler radar data. *J. Atmos. Sci.*, **62**, 351–370, doi:10.1175/JAS-3392.1.

Kingsmill, D. E., 1995: Convection initiation associated with a sea-breeze front, a gust front, and their collision. *Mon. Wea. Rev.*, **123**, 2913–2933, doi:10.1175/1520-0493(1995)123<2913:CIAWAS>2.0.CO;2.

Kosiba, K., J. Wurman, Y. Richardson, P. Markowski, P. Robinson, and J. Marquis, 2013: Genesis of the Goshen County, Wyoming, tornado on 5 June 2009 during VORTEX2. *Mon. Wea. Rev.*, **141**, 1157–1181, doi:10.1175/MWR-D-12-00056.1.

Kristovich, D. A. R., and Coauthors, 2000: The Lake-Induced Convection Experiment (Lake-ICE) and the Snowband Dynamics Project. *Bull. Amer. Meteor. Soc.*, **81**, 519–542, doi:10.1175/1520-0477(2000)081<0519:TLCEAT>2.3.CO;2.

——, and Coauthors, 2017: The Ontario Winter Lake-effect Systems (OWLeS) field project: Scientific and educational adventures to further our knowledge and prediction of lake-effect storms. *Bull. Amer. Meteor. Soc.*, **98**, 315–332, doi:10.1175/BAMS-D-15-00034.1.

Laird, N. F., L. J. Miller, and D. A. R. Kristovich, 2001: Synthetic dual-Doppler analysis of a winter mesoscale vortex. *Mon. Wea. Rev.*, **129**, 312–331, doi:10.1175/1520-0493(2001)129<0312:SDDAOA>2.0.CO;2.

Lee, B. D., and R. B. Wilhelmson, 1997: The numerical simulation of non-supercell tornadogenesis. Part I: Initiation and evolution of pretornadic misocyclone circulations along a dry outflow boundary. *J. Atmos. Sci.*, **54**, 32–60, doi:10.1175/1520-0469(1997)054<0032:TNSONS>2.0.CO;2.

Leslie, F. W., 1977: Surface roughness effects on suction vortex formation: A laboratory simulation. *J. Atmos. Sci.*, **34**, 1022–1027, doi:10.1175/1520-0469(1977)034<1022:SREOSV>2.0.CO;2.

Majcen, M., P. Markowski, Y. Richardson, D. Dowell, and J. Wurman, 2008: Multipass objective analysis of Doppler radar data. *J. Atmos. Oceanic Technol.*, **25**, 1845–1858, doi:10.1175/2008JTECHA1089.1.

Markowski, P., and Y. Richardson, 2010: *Mesoscale Meteorology in Midlatitudes.* Wiley-Blackwell, 407 pp.

Marquis, J. N., Y. P. Richardson, and J. M. Wurman, 2007: Kinematic observations of misocyclones along boundaries during IHOP. *Mon. Wea. Rev.*, **135**, 1749–1768, doi:10.1175/MWR3367.1.

Minder, J. R., T. W. Letcher, L. S. Campbell, P. V. Veals, and W. J. Steenburgh, 2015: The evolution of lake-effect convection during landfall and orographic uplift as observed by profiling radars. *Mon. Wea. Rev.*, **143**, 4422–4442, doi:10.1175/MWR-D-15-0117.1.

Mueller, C. K., and R. E. Carbone, 1987: Dynamics of a thunderstorm outflow. *J. Atmos. Sci.*, **44**, 1879–1898, doi:10.1175/1520-0469(1987)044<1879:DOATO>2.0.CO;2.

Niziol, T. A., 1987: Operational forecasting of lake effect snowfall in western and central New York. *Wea. Forecasting*, **2**, 310–321, doi:10.1175/1520-0434(1987)002<0310:OFOLES>2.0.CO;2.

——, W. R. Snyder, and J. S. Waldstreicher, 1995: Winter weather forecasting throughout the eastern United States. Part IV: Lake effect snow. *Wea. Forecasting*, **10**, 61–77, doi:10.1175/1520-0434(1995)010<0061:WWFTTE>2.0.CO;2.

Pauley, P. M., and X. Wu, 1990: The theoretical, discrete, and actual response of the Barnes objective analysis scheme for one- and two-dimensional fields. *Mon. Wea. Rev.*, **118**, 1145–1163, doi:10.1175/1520-0493(1990)118<1145:TTDAAR>2.0.CO;2.

Phillips, D. W., 1972: Modification of surface air over Lake Ontario in winter. *Mon. Wea. Rev.*, **100**, 662–670, doi:10.1175/1520-0493(1972)100<0662:MOSAOL>2.3.CO;2.

Rayleigh, L., 1880: On the stability, or instability, of certain fluid motions. *Proc. London Math. Soc.*, **XI**, 57–70.

Reinking, R. F., and Coauthors, 1993: The Lake Ontario Winter Storms (LOWS) project. *Bull. Amer. Meteor. Soc.*, **74**, 1828–1849, doi:10.1175/1520-0477-74-10-1828.

Rodi, A., 2011: King of the air: The evolution and capabilities of Wyoming's observations aircraft. *Meteorological Technology International*, May 2011, UKIP, Dorking, United Kingdom, 44–47.

Rodriguez, Y., D. A. R. Kristovich, and M. R. Hjelmfelt, 2007: Lake-to-lake cloud bands: Frequencies and locations. *Mon. Wea. Rev.*, **135**, 4202–4213, doi:10.1175/2007MWR1960.1.

Unauthenticated | Downloaded 02/02/24 12:11 AM UTC

Shin, H. H., and S.-Y. Hong, 2015: Representation of the subgrid-scale turbulent transport in convective boundary layers at gray-zone resolutions. *Mon. Wea. Rev.*, **143**, 250–271, doi:10.1175/MWR-D-14-00116.1.

Skamarock, W. C., 2004: Evaluating mesoscale NWP models using kinetic energy spectra. *Mon. Wea. Rev.*, **132**, 3019–3032, doi:10.1175/MWR2830.1.

Smirnova, T. G., J. M. Brown, S. G. Benjamin, and J. S. Kenyon, 2016: Modifications to the Rapid Update Cycle land surface model (RUC LSM) available in the Weather Research and Forecasting (WRF) Model. *Mon. Wea. Rev.*, **144**, 1851–1865, doi:10.1175/MWR-D-15-0198.1.

Sousounis, P. J., and G. E. Mann, 2000: Lake-aggregate mesoscale disturbances. Part V: Impacts on lake-effect precipitation. *Mon. Wea. Rev.*, **128**, 728–745, doi:10.1175/1520-0493(2000)128<0728:LAMDPV>2.0.CO;2.

Steiger, S. M., and R. J. Ballentine, 2008: Structure and characteristics of long lake-axis-parallel lake-effect storms. *24th Conf. on Severe Local Storms*, Savannah, GA, Amer. Meteor. Soc., 13B.6. [Available online at https://ams.confex.com/ams/24SLS/techprogram/paper_142021.htm.]

——, and Coauthors, 2013: Circulations, bounded weak echo regions, and horizontal vortices observed within long-lake-axis-parallel–lake-effect storms by the Doppler on Wheels. *Mon. Wea. Rev.*, **141**, 2821–2840, doi:10.1175/MWR-D-12-00226.1.

Thompson, G., P. R. Field, R. M. Rasmussen, and W. D. Hall, 2008: Explicit forecasts of winter precipitation using an improved bulk microphysics scheme. Part II: Implementation of a new snow parameterization. *Mon. Wea. Rev.*, **136**, 5095–5115, doi:10.1175/2008MWR2387.1.

Wheatley, D. M., and R. J. Trapp, 2008: The effect of mesoscale heterogeneity on the genesis and structure of mesovortices within quasi-linear convective systems. *Mon. Wea. Rev.*, **136**, 4220–4241, doi:10.1175/2008MWR2294.1.

Wilczak, J., D. Wolfe, R. Zamora, B. Stankov, and T. Christian, 1992: Observations of a Colorado tornado. Part I: Mesoscale environment and tornadogenesis. *Mon. Wea. Rev.*, **120**, 497–521, doi:10.1175/1520-0493(1992)120<0497:OOACTP>2.0.CO;2.

Wilson, J. W., G. B. Foote, N. A. Crook, J. C. Frankhauser, C. G. Wade, J. D. Tuttle, C. K. Mueller, and S. K. Krueger, 1992: The role of boundary-layer convergence zones and horizontal rolls in the initiation of thunderstorms: A case study. *Mon. Wea. Rev.*, **120**, 1785–1815, doi:10.1175/1520-0493(1992)120,1785:TROBLC.2.0.CO;2.

Wittenberg, A. T., 2009: Are historical records sufficient to constrain ENSO simulations? *Geophys. Res. Lett.*, **36**, L12702, doi:10.1029/2009GL038710.

Wurman, J., J. Straka, E. Rasmussen, M. Randall, and A. Zahrai, 1997: Design and deployment of a portable, pencil-beam, pulsed, 3-cm Doppler radar. *J. Atmos. Oceanic Technol.*, **14**, 1502–1512, doi:10.1175/1520-0426(1997)014<1502:DADOAP>2.0.CO;2.

Unauthenticated | Downloaded 02/02/24 12:11 AM UTC